NOVA SCHOOL OF SCIENCE & TECHNOLOGY

DEPARTMENT OF PHYSICS

MIGUEL CARMONA OLIVEIRA FERRO

Bachelor of Science in Physics Engineering

MODELING AND OPTIMIZATION OF LASER SPECTROSCOPY OF THE HYPERFINE GROUND STATE IN MUONIC HYDROGEN

MASTER IN PHYSICS ENGINEERING

NOVA University Lisbon
November, 2021

NOVA SCHOOL OF SCIENCE & TECHNOLOGY

DEPARTMENT OF PHYSICS

MODELING AND OPTIMIZATION OF LASER SPECTROSCOPY OF THE HYPERFINE GROUND STATE IN MUONIC HYDROGEN

MIGUEL CARMONA OLIVEIRA FERRO

Bachelor of Science in Physics Engineering

Supervisor: Pedro Amaro
Assistant Professor, NOVA University Lisbon

Co-supervisor: Aldo Antognini
Dr, ETH Zürich

Examination Committee:

Chair: André Wemans
Assistant Professor, NOVA University Lisbon

Rapporteur: José Marques
Associate Professor, Faculdade de Ciências da Universidade de Lisboa

Superisor: Pedro Amaro
Assistant Professor, NOVA University Lisbon

MASTER IN PHYSICS ENGINEERING

NOVA University Lisbon
November, 2021

Modeling and Optimization of Laser Spectroscopy of the Hyperfine Ground State in Muonic Hydrogen

This document was created using the (pdf/Xe/Lua)LaTeX processor, based on the NOVAthesis template, developed at the Dep. Informática of FCT-NOVA by João M. Lourenço. [1]

Acknowledgements

This thesis would not be possible without the tireless help of my supervisor, Professor Pedro Amaro, by whom no question, however small it may have appeared, was ever deemed unworthy of genuine attention. I would also like to thank my co-supervisor, Dr. Aldo Antognini, for trusting that this work could possibly be valuable to such a large-scale collaboration.

My family has always been the never-ending source of encouragement and drive moving me forward, and it goes without saying that this work is partially theirs, since without their support I would not be where I am today. A special thank you to my grandparents for their unconditional love during five years of shared accommodation, which felt like living with my parents and best friends at the same time.

A big thank you goes out to all the friends and colleagues who made these five years a bearable, enjoyable, fun, and (sometimes) productive experience, with a special mention to the one friend who turned the last three of these years into the best ones of my life.

Lastly, I would like to thank NOVA-SST (former FCT-UNL) and all it's professors and staff members with whom I crossed paths with, for making me feel at home while allowing and helping me to learn as much as possible.

"One man can make a difference and every man should try."
(Jacqueline Kennedy Onassis)

Abstract

The upcoming HyperMu experiment from the CREMA collaboration aims for a measurement of the ground-state hyperfine splitting (HFS) in muonic hydrogen (μp) by means of pulsed laser spectroscopy as a new route for probing the fine details of proton nuclear structure. In the proposed experimental scheme, the transition from the singlet to the triplet hyperfine state is driven by laser excitation and the excited μp atoms are afterwards quenched back to the singlet state through inelastic collisions with H_2 molecules. The kinetic energy increase of the μp atoms after collisional de-excitation greatly increases their probability of detection within the muon's lifetime, and the population of collisionally quenched μp atoms is therefore used as a model for the probability of a successful detection.

In this work a simulation method was developed in order to calculate the combined probability of laser excitation followed by collisional de-excitation of a μp atom under different sets of possible experimental conditions, such as temperature, pressure, laser pulse fluence and time duration and cavity mirror reflectivity and diameter. The implemented simulation allows the calculation of this combined probability from the optical Bloch equations, which were derived for an electric field dependent on the laser and cavity conditions, while also accounting for collisional and Doppler effects. The combined probability was calculated for several sets of different experimental parameters, thus providing a new and alternative method for the optimization of both the temperature and pressure of the H_2 gas, where the μp atoms undergo laser excitation, as well as the laser and cavity conditions.

Keywords: Muonic atoms, Hyperfine structure, Laser excitation, Collisional quenching, Bloch equations, Simulation

Resumo

O projeto HyperMu, proposto pela colaboração CREMA, tem como objetivo a medição da separação hiperfina (HFS) do estado fundamental em átomos de hidrogénio muónico (μp) através de espectroscopia laser como medida alternativa para a investigação dos detalhes da estrutura nuclear do protão. De acordo com o esquema experimental proposto, a transição entre os estados hiperfinos singleto e tripleto é obtida através de excitação laser, sendo que os átomos de μp excitados regressam depois ao estado singleto por via de colisões inelásticas com moleculas de H_2. O acréscimo de energia cinética adquirido pelos átomos de μp após desexcitação aumenta significativamente a probabilidade de deteção durante o tempo de vida do muão. Como tal, a população de átomos de μp que atinge o estado de desexcitação é utilizada como modelo para a probabilidade de deteção no enquadramento desta experiência.

Neste trabalho foi desenvolvido um método de simulação para calcular a probabilidade combinada de excitação e subsequente desexcitação de um átomo de μp sob diferentes condições experimentais, tais como, temperatura, pressão, fluência e duração do pulso laser, reflectividade e distância entre espelhos da cavidade laser. A simulação desenvolvida permite o cálculo desta probabilidade através da resolução das equações ópticas de Bloch, que foram derivadas para um campo elétrico dependente das condições do pulso e da cavidade laser, incluíndo também os efeitos dos diferentes tipos de colisão e o efeito de Doppler. A probabilidade combinada de excitação foi calculada para diferentes valores de diversos parâmetros experimentais proporcionando um novo método de optimização das condições de temperatura e pressão do gás de H_2, onde os átomos de μp se encontram aquando da excitação laser, assim como das condições do pulso e da cavidade laser.

Palavras-chave: Átomos muónicos, Estrutura hiperfina, Excitação laser, Equações de Bloch, Simulação

Contents

List of Figures

List of Tables

Abbreviations

CREMA Charge Radius Experiments with Muonic Atoms (collaboration)

E1 electric dipole

FWHM full width at half maximum

HFS hyperfine splitting

JIT Just-In-Time (compiler)

M1 magnetic dipole

QCD quantum chromodynamics
QED quantum electrodynamics

ufunc universal function (C, Python)

Symbols

μp	muonic hydrogen
μ^2H	muonic deuterium
μ^4He	muonic helium-4
Z	atomic number
n	principal quantum number
L	orbital angular momentum quantum number
S	orbital spin quantum number
J	total orbital angular momentum quantum number
I	nuclear spin quantum number
F	total angular momentum quantum number
M_F	secondary total angular momentum quantum number
Ψ	total wavefunction
$\hat{\boldsymbol{H}}$	Hamiltonian operator
$\hat{\boldsymbol{H}}_A$	time-independent atomic Hamiltonian
$\hat{\boldsymbol{H}}_I$	time-dependent interaction Hamiltonian
$\hat{\boldsymbol{L}}$	orbital angular momentum operator
$\hat{\boldsymbol{S}}$	orbital spin angular momentum operator
$\hat{\boldsymbol{I}}$	nuclear spin angular momentum operator
$\hat{\boldsymbol{\mu}}$	magnetic moment operator
e	elementary charge
c	speed of light in vacuum
$\hbar$	reduced Planck's constant
k_B	Boltzmann's constant

ε_0	vacuum permittivity
m_μ	muon mass
m_p	proton mass
$m_{\mu\mathrm{p}}$	muonic hydrogen mass
g_p	proton g-factor
g_μ	muon g-factor
$\vec{E}$	electric field
E_0	electric field amplitude
$\mathcal{E}$	dimensionless Doppler-shifted electric field
$\vec{B}$	magnetic field
$\hat{k}$	direction of propagation of an electromagnetic wave
$\hat{\varepsilon}$	direction of polarization of the electric field
$\mathcal{M}$	transition matrix element
$\mathcal{M}_{\mathrm{M1}}$	magnetic dipole transition matrix element
T	temperature
P	pressure
D	laser cavity diameter
R	laser cavity reflectivity
τ	laser pulse duration
$\mathcal{I}$	laser intensity
$\mathcal{F}$	total laser fluence
$\overline{\mathcal{F}}$	average total laser fluence
$\mathcal{F}_0$	initial laser pulse fluence
$\mathcal{V}$	Rabi frequency
Ω	generalized Rabi frequency
ω_r	resonance frequency
ω_D	Doppler shift frequency
Δ	laser frequency detune
ρ_{ii}	population of the i-th state
ρ_{ij}	coherence between i-th and j-th states
ρ_{11}	population of the 1S($F = 0$) state of μp
ρ_{22}	population of the 1S($F = 1$) state of μp

ρ_{33}	population of the collisionally quenched 1S($F = 0$) state of μp
$\overline{\rho_{33}}$	average population of the collisionally quenched 1S($F = 0$) state of μp
Γ_{sp}	rate of spontaneous emission
Γ_{el}	rate of elastic collisions
Γ_{inel}	rate of inelastic collisions
Γ_D	width of the Doppler shift probability distribution
Γ_c	decay rate of the coherence terms (decoherence rate)
$\vec{v}$	velocity
v_x	x-component of velocity
E_{kin}	kinetic energy
γ	photon
i	imaginary unit
c.c	complex conjugate

1

Introduction

1.1 Context and motivation

According to the Standard Model of Elementary Particles, the second generation of leptons with electric charge is known as a *muon*. This elementary particle has the same electric charge and spin as the electron, but has a mass 200 times greater. Muonic atoms (a bound system of a muon and a nucleus), such as muonic hydrogen (μp), are significantly more compact (factor of $\sim 1/200$) than their respective (more common) 'electronic' atom [2] due to the much larger mass of the orbiting particle. Therefore, since the volume overlap of the muon's wavefunction with the nucleus is much higher (factor of $\sim 200^3$), their atomic structure is much more sensitive to the properties of the atomic nucleus. High-precision measurements of the muonic atomic structure can thus probe the properties of atomic nuclei related to their charge and magnetic distribution and polarizability [2–5].

Laser spectroscopy in μp has long been proposed as a route to probe the proton's size by a measurement of the frequency difference between the $2S_{1/2}$ and $2P_{1/2}$ states, known as the Lamb shift [2]. It took one decade for this measurement to be accomplished by the CREMA collaboration, leading to the most accurate measurement of the proton charge radius and, unexpectedly, to the proton radius puzzle [6, 7] which sparked new theoretical and experimental efforts. Since then, several experiments, theoretical investigations and re-analysis of previous measurements have been performed towards the measurement of the proton radius [8–15]. Most of these recent works favor the proton radius value as extracted from μp, despite some remaining tension between a few experimental results [16, 17].

After having performed laser spectroscopy of the Lamb shift in μp [6, 7], μ^2H [18] and μ^4He [19, 20], yielding the corresponding nuclear charge radii with unprecedented precision, the CREMA collaboration is now preparing a measurement of the ground-state hyperfine splitting (HFS) in μp with the HyperMu experiment [21]. These measurements present a new route towards the measurement of the proton's properties, namely the so called two-photon-exchange contribution which can be related to the Zemach radius

(a measure of both the proton's charge and magnetic nuclear structure) and an additional polarizability contribution. These physical quantities allow for a benchmark of phenomenological dispersion theories [22, 23] and state-of-the-art chiral perturbation theory [24–27], providing decisive insights about quantum chromodynamics (QCD) in the low energy regime, which cannot currently provide reliable predictions without experimental input [28–31].

1.2 Objective

In order to guide the optimization of experimental parameters, a theoretical evaluation of the laser excitation probability between the hyperfine sublevels at various experimental conditions is needed. Among the physical processes that influence this probability are the broadening of spectroscopic lines due to elastic and inelastic collisions, and the Doppler broadening caused by the velocity distribution of the μp atoms. On top of the mentioned broadening mechanisms, another aspect to consider is the effective shape of the electromagnetic field with which the μp atoms interact and how the parameters of the laser cavity influence the probability of laser excitation. The purpose of this thesis is to theoretically investigate these sources of broadening, while the μp atoms interact with the electromagnetic field inside the laser cavity, and their influence on the probability of laser excitation.

1.3 Layout

This thesis is organized into six chapters. The present chapter serves to provide the context and objective for this thesis' work and the remaining chapters are structured as follows:

- Chapter 2 introduces the HFS in μp and outlines the upcoming HyperMu experiment from the CREMA collaboration with a special focus on the proposed experimental scheme to be used;
- Chapter 3 presents the developed theoretical framework, based on the optical Bloch equations and the modeling of the laser's electric field in the proposed setup of the HyperMu experiment.
- Chapter 4 is dedicated to the simulation employed for the calculation of the excited μp populations based on the developed theoretical framework;
- Chapter 5 contains the obtained results and respective discussion;
- Chapter 6 is where the final conclusions are drawn.

2

The HyperMu Experiment

2.1 Hyperfine structure of the 1S state in muonic hydrogen

The hyperfine structure of the energy levels of an atom results from the interaction of its nuclear magnetic dipole moment, arising from the nuclear spin (I), with the electromagnetic field produced by the spin of its orbiting particle [32]. It contrasts with the fine structure of the energy levels, which arises from the interaction between the orbiting particle's spin (S) and angular momentum (L) and relativistic corrections to the non-relativistic Schrödinger equation [32].

The ground-state ($1S_{1/2}$) of a μp atom without HFS, is characterized by the quantum numbers

$$n = 1 \quad , \quad L = 0 \quad , \quad J = \frac{1}{2} \, , \tag{2.1}$$

where n is the principal quantum number and L and J are the orbital angular momentum and total angular momentum of the muon, respectively.

The proton is a spin-$\frac{1}{2}$ particle, i.e.,

$$I = \frac{1}{2} \, , \tag{2.2}$$

and the total angular momentum of the system, F, given by the coupling of the muon's total angular momentum and the proton's spin, takes the possible values [32]

$$|I - J| \leq F \leq I + J \, , \tag{2.3}$$

resulting in

$$F = 0, 1 \, , \tag{2.4}$$

which correspond to different alignments of the muon and the proton's magnetic moments and give rise to the ground-state HFS of μp represented in figure 2.1.

Each state F has a multiplicity given by $2F + 1$, with substates characterized by the quantum number M_F, taking the possible integer values in the range [32]

$$-F \leq M_F \leq F \, . \tag{2.5}$$

Given their multiplicity, the 1S($F = 0$) and 1S($F = 1$) are therefore referred to as the singlet and triplet states of the ground-state HFS, respectively.

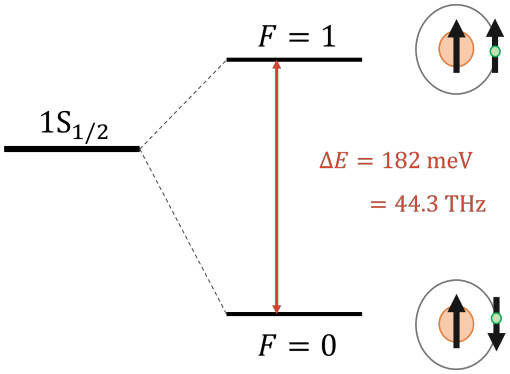

Figure 2.1: Representation of the ground-state HFS of μp into the singlet ($F = 0$) and triplet ($F = 1$) states. The arrows represent the alignments of the nuclear and orbital magnetic dipole moments. HFS energy taken from [33].

2.1.1 Magnetic dipole interaction

The HFS transition between the 1S($F = 0$) and 1S($F = 1$) states is forbidden under the electric dipole (E1) selection rules, given that $\Delta L = 0$ and both states have $L = 0$ [32]. It is, however, possible under the magnetic dipole (M1) selection rules, therefore classifying as an M1 transition [32, 34] which can be excited through the interaction of the muon's magnetic dipole moment with an applied electromagnetic field.

In the presence of an external magnetic field ($\vec{B}$), a bound particle of an atom acquires a potential energy given by the Hamiltonian [32]

$$\hat{\boldsymbol{H}}_{\mathrm{M1}} = -\hat{\boldsymbol{\mu}} \cdot \vec{B} \, , \tag{2.6}$$

where $\hat{\boldsymbol{\mu}}$ is the magnetic moment operator. Considering the case of the μp atom, this operator takes the form [33, 34]

$$\hat{\boldsymbol{\mu}}_{\mu\mathrm{p}} = -\frac{e}{2m_\mu}\left(\hat{\boldsymbol{L}} + g_\mu \hat{\boldsymbol{S}} + g_{\mathrm{p}} \frac{m_\mu}{m_{\mathrm{p}}} \hat{\boldsymbol{I}}\right) , \tag{2.7}$$

where m_μ and m_p are the muon and the proton's masses, respectively, e is the elementary charge, $\hat{\boldsymbol{L}}$ is the muon's orbital angular momentum operator, $\hat{\boldsymbol{S}}$ and $\hat{\boldsymbol{I}}$ are the spin angular momentum operators for the muon and the proton, respectively and g_μ and g_{p} are the g-factors for the muon (≈ 2.00) and the proton (≈ 5.58), respectively. In the transition $1S(F = 0) \rightarrow 1S(F = 1)$, both the initial and final states have $L = 0$, leading to

$$\hat{\boldsymbol{\mu}}_{\mu\mathrm{p}} = -\frac{e}{2m_\mu}\left(g_\mu \hat{\boldsymbol{S}} + g_\mathrm{p}\frac{m_\mu}{m_\mathrm{p}}\hat{\boldsymbol{I}}\right) . \tag{2.8}$$

The applied magnetic field has an associated electric field, $\vec{E}$, given by [35]

$$\vec{E} = E_0 \cos(\omega t)\hat{\varepsilon} , \tag{2.9}$$

and can therefore be written as

$$\vec{B} = \frac{E_0}{c}\cos(\omega t)(\hat{k}\times\hat{\varepsilon}) , \tag{2.10}$$

where $\hat{k}$ is the direction of propagation and $\hat{\varepsilon}$ represents the electric field polarization.

With the use of equations (2.7) and (2.10), the Hamiltonian of equation (2.6) becomes

$$\hat{\boldsymbol{H}}_{\mathrm{M1}} = \frac{eE_0}{2m_\mu c}\left(g_\mu \hat{\boldsymbol{S}} + g_\mathrm{p}\frac{m_\mu}{m_\mathrm{p}}\hat{\boldsymbol{I}}\right)\cdot(\hat{k}\times\hat{\varepsilon})\cos(\omega t) \tag{2.11}$$

and the corresponding matrix element for a transition between an initial state $|F=0, M_F=0\rangle$ and a final state $|F'=1, M_F'\rangle$ is given, in m^{-1}, by [33]

$$\mathcal{M}_{\mathrm{M1}}^{(0,M_F')} = \frac{1}{2m_\mu c}\left\langle F'=1, M_F' \left| \left(g_\mu \hat{\boldsymbol{S}} + g_\mathrm{p}\frac{m_\mu}{m_\mathrm{p}}\hat{\boldsymbol{I}}\right)\cdot(\hat{k}\times\hat{\varepsilon}) \right| F=0, M_F=0 \right\rangle . \tag{2.12}$$

In the transition between the $1\mathrm{S}(F=0)$ and $1\mathrm{S}(F=1)$ states, the exact distribution between each possible M_F substate is determined by the laser polarization $\hat{\varepsilon}$. In this work the population distribution between each of these substates and the related effects of laser polarization are neglected. A study on the role of laser polarization in spectroscopy of the ground-state HFS transition in μp can be found in [36]. The magnetic dipole matrix element, $\mathcal{M}_{\mathrm{M1}}$, is thus given by the sum over possible M_F' states [33, 34]

$$\mathcal{M}_{\mathrm{M1}}^2 = \sum_{M_F'} \left|\mathcal{M}^{(0,M_F')}\right|^2 \tag{2.13}$$

and its value is presented in table 2.1. The matrix element for the E1 transition between the $2\mathrm{S}_{1/2}(F=1)$ and the $2\mathrm{P}_{3/2}(F=2)$ states of μp, used in the Lamb shift experiments, is also presented for comparison.

Table 2.1: Matrix elements for the $2\mathrm{S}(F=1)\rightarrow 2\mathrm{P}(F=2)$ and $1\mathrm{S}(F=0)\rightarrow 1\mathrm{S}(F=1)$ transitions in μp. Values taken from [33, 37].

Transition	Transition type	$\mathcal{M}$ [m]	Lifetime [s]
$2\mathrm{S}(F=1)\longrightarrow 2\mathrm{P}(F=2)$	E1	6.367×10^{-13}	8.5×10^{-12}
$1\mathrm{S}(F=0)\longrightarrow 1\mathrm{S}(F=1)$	M1	1.228×10^{-15}	8.1×10^{4}

2.2 Experimental scheme

The goal of the CREMA collaboration is to measure the ground-state HFS in μp, represented in figure 2.1, by means of pulsed laser spectroscopy. From this measurement the nuclear structure effects on the energy of the ground-state HFS will be determined with a relative accuracy of 10^{-4}, from which the proton's Zemach radius can be extracted with a relative accuracy of 0.25% [37].

The proposed experiment will consist of three main stages [38], represented in figure 2.2 and ordered as follows:

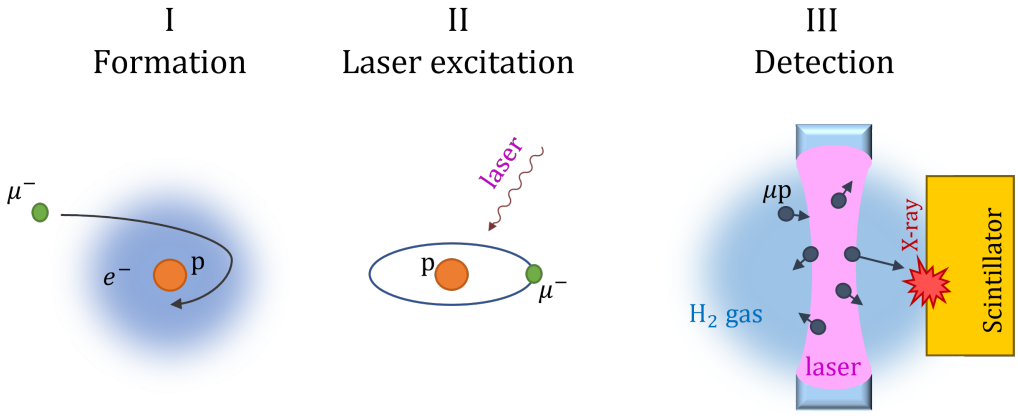

Figure 2.2: Representation of the three main stages of the μp HFS experiment. Adapted from [38].

1. **Muonic hydrogen formation** - Low energy muons are stopped in a cryogenic (T = 22 K) H_2 gas target at 0.5 bar pressure leading to the formation of μp atoms in highly excited states that quickly de-excite to the singlet state, acquiring some kinetic energy in the process (up to 100 eV). The formed μp atoms collide with the residual H_2 gas molecules and reach thermal equilibrium in about 1 μs [33].

2. **Laser excitation** - A laser pulse of 44.3 THz frequency induces the hyperfine transition

$$\mu\mathrm{p}(F=0)+\gamma \longrightarrow \mu\mathrm{p}(F=1)\,, \tag{2.14}$$

   where γ represents a laser photon.

   To maximize the probability of excitation, the μp atoms are formed inside a high-reflectivity multipass laser cavity in which the emitted laser pulse is successively reflected, maximizing its intensity. The theoretical modeling of the laser's electric field, developed in section 3.3, takes into account the multiple reflections inside the laser cavity.

3. **Detection** -The excited μp atoms collide with the H_2 gas molecules with the possibility of being quenched back to the singlet state in a process described by the de-excitation reaction

$$\mu p(F=1) + H_2 \longrightarrow \mu p(F=0) + E_{kin} + H_2 \,, \tag{2.15}$$

where part of the HFS transition energy is converted into kinetic energy (E_{kin}) acquired by the μp atoms. The faster moving de-excited μp atoms are able to reach the target walls before decaying. The walls are coated with a high-Z material so that upon reaching the walls, the muon is transferred from the μp atom to a high-Z atom in highly excited states. The muon transfer to a highly excited state will result in a cascade of de-excitations with emission of X-rays. A resonance curve is retrieved where the number of emitted X-rays is plotted against the applied laser frequency.

The focus of this work lies within the last two stages described, particularly in the interaction of the μp atoms with the laser and the H_2 gas inside the cavity represented in figure 2.3.

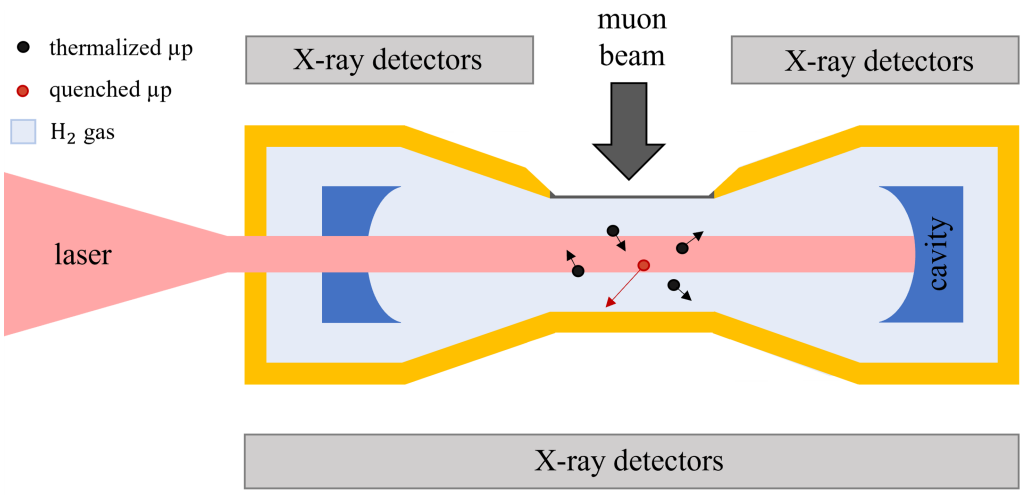

Figure 2.3: Schematic of the HyperMu experimental setup. Adapted from [33].

2.3 Comparison with Lamb shift measurements

The Lamb shift is the energy difference between the $2S_{1/2}$ and $2P_{1/2}$ energy levels in an hydrogenlike atoms [39], resulting mainly from radiative effects described by quantum electrodynamics (QED), such as *self energy* and *vacuum polarization* [3]. One other contribution for the Lamb shift is given by the finite size of the atomic nucleus [40] and it is significantly enhanced in μp, given ts much smaller atomic Bohr radius relative to that of a regular hydrogen atom [4]. Based on this principle, the previous measurements of the proton radius obtained with μp, performed by the CREMA collaboration [6, 7], are

based on the measurement of the 2S-2P transitions, following the energy level scheme and experimental principle represented in figure 2.4.

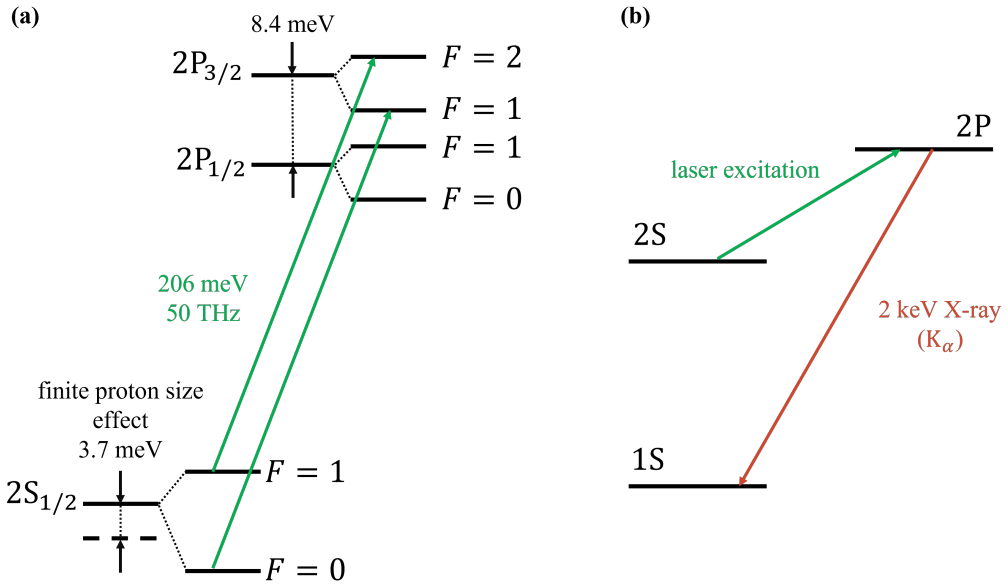

Figure 2.4: Experimental principle in the measurement of the Lamb shift in μp. Adapted from [6]. **(a)** - Lamb shift in μp with representation of the proton's finite size contribution. The green arrows represent the laser excited transitions. **(b)** - Laser excitation and detection principles. When the laser is on resonance with the desired transition, delayed K_α X-rays are observed.

Even though the HyperMu experiment shares the purpose of the μp Lamb shift experiments from the CREMA collaboration, which is to probe the nuclear properties via laser spectroscopy of muonic atoms [6, 7], it contains relevant distinctions in both the atomic transitions and detection methods, namely:

- In the Lamb shift experiments, the measurement of the 2S-2P transitions gives information on the proton *charge radius* [6, 7]. Differently, the HFS of μp, represented in figure 2.1, arises from the interaction between the magnetic moments of the muon and the nucleus and provides information about the *magnetic structure* of the proton.

- While a prompt X-ray from the excited state is emitted as signature of an event in the Lamb shift experiments (see figure 2.4), in the HyperMu experiment the excited HFS state is metastable, with a lifetime millions of times larger than the muon decay time (~ 2 μs), given the much smaller transition matrix element (see table 2.1). This, in turn, makes fluorescent radiation extremely difficult to observe [21]. Therefore, an alternative method of detection (described in section 3.2) was proposed, in which the excited μp atoms are de-excited through inelastic collisions with H_2 gas molecules being afterwards detected with the use of high-Z scintillators, as represented in figures 2.2 and 2.3.

3

Theoretical Framework

3.1 Time evolution of the two-level system

The time evolution of a quantum system with two possible energy levels, such as the singlet and triplet states obtained from the ground state HFS of μp, can be described by time-dependent quantum mechanics through the *optical Bloch equations* [41].

In a quantum mechanical treatment, the time evolution of the system is given by the time-dependent Schrödinger equation

$$i\hbar\frac{\mathrm{d}\Psi}{\mathrm{d}t} = \hat{\boldsymbol{H}}\Psi \ , \tag{3.1}$$

where Ψ and $\hat{\boldsymbol{H}}$ are the total wavefunction and the Hamiltonian of the system, respectively, $\hbar$ is the reduced Planck constant and i is the imaginary unit.

When in interaction with an external field, the overall wavefunction is given by a superposition of the two possible states, Ψ_1 and Ψ_2, as

$$\Psi(\vec{r},t) = C_1(t)\Psi_1(\vec{r},t) + C_2(t)\Psi(\vec{r},t) \ . \tag{3.2}$$

The Hamiltonian of the atomic system is given by

$$\hat{\boldsymbol{H}} = \hat{\boldsymbol{H}}_A + \hat{\boldsymbol{H}}_I(t) \ , \tag{3.3}$$

where $\hat{\boldsymbol{H}}_A$ represents the time-independent Hamiltonian with the kinetic and potential energy of the bound particles, and $\hat{\boldsymbol{H}}_I$ represents the time-dependent interaction of the atom with the external field. Equations (3.1), (3.2) and (3.3) produce the following equations of motion

$$i\hbar\frac{dC_1}{dt} = \langle 1|\hat{\boldsymbol{H}}_I|1\rangle C_1 + \exp(-i\omega_r t)\langle 1|\hat{\boldsymbol{H}}_I|2\rangle C_2 \ , \tag{3.4}$$

$$i\hbar\frac{dC_2}{dt} = \langle 2|\hat{\boldsymbol{H}}_I|2\rangle C_2 + \exp(i\omega_r t)\langle 2|\hat{\boldsymbol{H}}_I|1\rangle C_1 \ , \tag{3.5}$$

where $|1\rangle$ and $|2\rangle$ represent the time-independent wavefunctions of each state, such that

$$\hat{\boldsymbol{H}}_{\boldsymbol{A}}|1\rangle = E_1|1\rangle \quad , \quad \hat{\boldsymbol{H}}_{\boldsymbol{A}}|2\rangle = E_2|2\rangle \ , \tag{3.6}$$

$$\Psi_1(\vec{r},t) = \exp\left(-i\frac{E_1}{\hbar}t\right)|1\rangle \quad , \quad \Psi_2(\vec{r},t) = \exp\left(-i\frac{E_2}{\hbar}t\right)|2\rangle \ , \tag{3.7}$$

and ω_r is the transition resonance frequency, defined as

$$\omega_r = \frac{E_2 - E_1}{\hbar} \ . \tag{3.8}$$

Instead of solving equations (3.4) and (3.5) with respect to the complex coefficients C_1 and C_2, a more convenient set of quantities is obtained with the density matrix

$$\begin{pmatrix} \rho_{11} & \rho_{12} \\ \rho_{21} & \rho_{22} \end{pmatrix} = \begin{pmatrix} |C_1|^2 & C_1 C_2^* \\ C_2 C_1^* & |C_2|^2 \end{pmatrix} , \tag{3.9}$$

following a physical interpretation in which the diagonal terms, ρ_{ii}, represent the *population* of each state and the off-diagonal terms, ρ_{ij}, represent the *coherence* of the population states [41]. Then, for a set of N atoms,

$$\rho_{11} = |C_1|^2 = N_1/N \quad , \quad \rho_{22} = |C_2|^2 = N_2/N \quad , \quad \rho_{11} + \rho_{22} = 1 \ , \tag{3.10}$$

where N_1 and N_2 represent the number of atoms in state 1 and 2, respectively.

The time evolution of the density matrix elements is given by

$$\frac{\mathrm{d}\rho_{ij}}{\mathrm{d}t} = C_i \frac{\mathrm{d}C_j^*}{\mathrm{d}t} + \frac{\mathrm{d}C_i}{\mathrm{d}t} C_j^* \ , \tag{3.11}$$

which, with the use of equations (3.4) and (3.5), produces the system of equations

$$\begin{aligned} \frac{\mathrm{d}\rho_{11}}{\mathrm{d}t} &= -\frac{\mathrm{d}\rho_{22}}{\mathrm{d}t} = \frac{i}{\hbar}\left[\rho_{12}\exp(i\omega_r t)\langle 2|\hat{\boldsymbol{H}}_I|1\rangle + \rho_{11}\langle 1|\hat{\boldsymbol{H}}_I|1\rangle^*\right] + \text{c.c} \ , \\ \frac{\mathrm{d}\rho_{12}}{\mathrm{d}t} &= \frac{\mathrm{d}\rho_{21}^*}{\mathrm{d}t} = \frac{i}{\hbar}\Big[\exp(-i\omega_r t)\Big(\rho_{11}\langle 2|\hat{\boldsymbol{H}}_I|1\rangle^* - \rho_{22}\langle 1|\hat{\boldsymbol{H}}_I|2\rangle\Big) + \rho_{12}\Big(\langle 2|\hat{\boldsymbol{H}}_I|2\rangle^* - \langle 1|\hat{\boldsymbol{H}}_I|1\rangle\Big)\Big] \ . \end{aligned} \tag{3.12}$$

where c.c stands for the complex conjugate of the preceding term. These equations describe the time evolution of a two-level system governed uniquely by stimulated excitation and emission. In order to solve these equations it is only required that the transition matrix elements of the interaction Hamiltonian in the two-level basis are known.

3.1.1 Optical Bloch equations

Considering the two-level system as a model for two possible energy levels of a bound particle in an atom, the interaction Hamiltonian terms take the form [41]

$$\langle 2|\hat{\boldsymbol{H}}_I|1\rangle = eE_0\mathcal{M}\cos(\omega t) \ , \tag{3.13}$$

where $\mathcal{M}$ represents a generic transition matrix element (in m^{-1}). For the HFS transition in μp the matrix element is given by equations (2.12) and (2.13) as

$$\mathcal{M}^2 = \frac{1}{4m_\mu^2 c^2} \sum_{M_F'} \left| \left\langle F' = 1, M_F' \left| \left(g_\mu \hat{\boldsymbol{S}} + g_\mathrm{p} \frac{m_\mu}{m_\mathrm{p}} \hat{\boldsymbol{I}} \right) \cdot (\hat{k} \times \hat{\varepsilon}) \right| F = 0, M_F = 0 \right\rangle \right|^2 . \tag{3.14}$$

The system of equations (3.12) becomes

$$\begin{aligned} \frac{\mathrm{d}\rho_{11}}{\mathrm{d}t} &= -\frac{\mathrm{d}\rho_{22}}{\mathrm{d}t} = i\mathcal{V}\cos(\omega t)\exp(i\omega_r t)\rho_{12} + \mathrm{c.c} \ , \\ \frac{\mathrm{d}\rho_{12}}{\mathrm{d}t} &= \frac{\mathrm{d}\rho_{21}^*}{\mathrm{d}t} = i\mathcal{V}^*\cos(\omega t)\exp(-i\omega_r t)(\rho_{11} - \rho_{22}) \ , \end{aligned} \tag{3.15}$$

where $\mathcal{V}$ is the *Rabi frequency*, defined as

$$\mathcal{V} = \frac{eE_0}{\hbar}\mathcal{M} . \tag{3.16}$$

This is the frequency at which the populations of the two-level system oscillate for a resonant excitation, i.e when $\omega = \omega_r$. It is dependent on both the amplitude of the excitation (laser intensity), given by the electric field amplitude E_0, and the response of the atomic system to the excitation, given by the transition matrix element $\mathcal{M}$.

The general system of (3.15) can be further simplified with the use of the *rotating-wave approximation* [41, 42], valid when $\omega \sim \omega_r$ and $\mathcal{V} \ll \omega$, where the terms oscillating with frequency $\omega_r + \omega$ are neglected and only those oscillating with frequency $\Delta = \omega_r - \omega$ are considered to produce variations on the energy level populations. With this approximation the system takes the form

$$\begin{aligned} \frac{\mathrm{d}\rho_{11}}{\mathrm{d}t} &= -\frac{\mathrm{d}\rho_{22}}{\mathrm{d}t} = \frac{i}{2}\mathcal{V}\rho_{12}e^{i\Delta t} + \mathrm{c.c} \ , \\ \frac{\mathrm{d}\rho_{12}}{\mathrm{d}t} &= \frac{\mathrm{d}\rho_{21}^*}{\mathrm{d}t} = \frac{i}{2}\mathcal{V}^* e^{-i\Delta t}(\rho_{11} - \rho_{22}) \ , \end{aligned} \tag{3.17}$$

where Δ represents the laser frequency detuning.

Introducing the substitutions

$$\rho_{12}e^{i\Delta t} \to \rho_{12} \qquad , \qquad \rho_{21}e^{-i\Delta t} \to \rho_{21} \ , \tag{3.18}$$

into the system of equations (3.17) we obtain

$$\begin{aligned} \frac{\mathrm{d}\rho_{11}}{\mathrm{d}t} &= -\frac{\mathrm{d}\rho_{22}}{\mathrm{d}t} = \frac{i}{2}\mathcal{V}\rho_{12} + \mathrm{c.c} \ , \\ \frac{\mathrm{d}\rho_{12}}{\mathrm{d}t} &= \frac{\mathrm{d}\rho_{21}^*}{\mathrm{d}t} = \frac{i}{2}\mathcal{V}^*(\rho_{11} - \rho_{22}) + i\Delta\rho_{12} \ , \end{aligned} \tag{3.19}$$

which correspond to the *optical Bloch equations* for a two-level system [41, 42]. These equations are equivalent to those of system (3.12), for an atomic two-level system with the generic matrix element of equation (3.13)

The Bloch equations defined in (3.19) are generally solved in the matrix form

$$\frac{\mathrm{d}\boldsymbol{\rho}}{\mathrm{d}t} = \boldsymbol{M}\boldsymbol{\rho} \,, \tag{3.20}$$

with

$$\boldsymbol{\rho} = \begin{pmatrix} \rho_{11} \\ \rho_{22} \\ \rho_{12} \\ \rho_{21} \end{pmatrix} \quad , \quad \boldsymbol{M} = \begin{pmatrix} 0 & 0 & i\frac{\mathcal{V}}{2} & -i\frac{\mathcal{V}^*}{2} \\ 0 & 0 & -i\frac{\mathcal{V}}{2} & i\frac{\mathcal{V}^*}{2} \\ i\frac{\mathcal{V}^*}{2} & -i\frac{\mathcal{V}^*}{2} & i\Delta & 0 \\ -i\frac{\mathcal{V}}{2} & i\frac{\mathcal{V}}{2} & 0 & -i\Delta \end{pmatrix} . \tag{3.21}$$

To find the solutions of the system, the eigenvalues of $\boldsymbol{M}$ can be calculated through

$$\det(\boldsymbol{M} - \lambda) = 0 \,, \tag{3.22}$$

with solutions

$$\lambda = 0, \pm i\Omega \,, \tag{3.23}$$

where

$$\Omega = \sqrt{\Delta^2 + |\mathcal{V}|^2} \,, \tag{3.24}$$

is the *generalized Rabi frequency* of the system, a generalization of the previously defined Rabi frequency of equation (3.16) for any value of the excitation frequency ω.

From equation (3.23) we obtain the general solutions

$$\rho_{ij} = A_{ij} + B_{ij}\exp(i\Omega t) + C_{ij}\exp(-i\Omega t) \qquad \text{with} \quad A_{ij}, B_{ij}, C_{ij} \in \mathbb{C} \,, \tag{3.25}$$

where the coefficients A_{ij}, B_{ij} and C_{ij} are determined by the initial conditions of the system. For the specific case of

$$\rho_{11}(0) = 1 \quad , \quad \rho_{22}(0) = 0 \quad , \quad \rho_{12}(0) = \rho_{12}(0) = 0 \,, \tag{3.26}$$

where all atoms are assumed to be in the ground state at $t = 0$, we obtain the solutions

$$\rho_{22} = \left(\frac{|\mathcal{V}|}{\Omega}\right)^2 \sin^2\left(\frac{1}{2}\Omega t\right) , \tag{3.27}$$

$$\rho_{12} = \left(\frac{|\mathcal{V}|}{\Omega^2}\right)\sin\left(\frac{1}{2}\Omega t\right)\left[-\Delta\sin\left(\frac{1}{2}\Omega t\right) + i\Omega\cos\left(\frac{1}{2}\Omega t\right)\right] , \tag{3.28}$$

plotted in figure 3.1 for different values of the detune ratio $\Delta/|\mathcal{V}|$. The observed oscillations of frequency Ω are called *Rabi oscillations* and their amplitude is determined by the detune ratio.

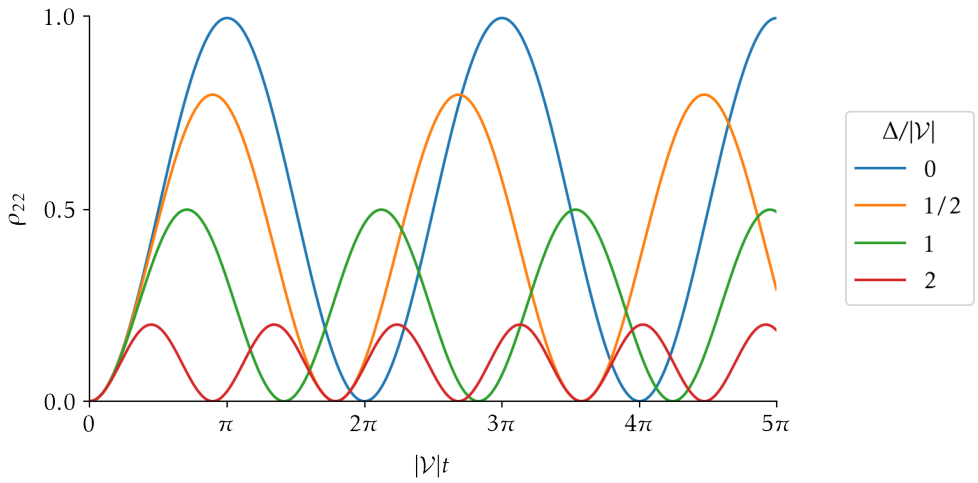

Figure 3.1: Time evolution of the ρ_{22} population, described by equation (3.27), for different values of the detune ratio $\Delta/|\mathcal{V}|$.

3.2 Broadening sources

3.2.1 Spontaneous emission

When a bound particle of an atom occupies an excited energy level it can spontaneously decay towards a lower energy level, emitting a photon [32]. This process of spontaneous emission has a given probability of occurrence, extracted from the transition matrix elements, and therefore an associated rate [41]. A diagram for an atomic two-level system with the inclusion of spontaneous emission, in addition to the processes of laser excitation and de-excitation, is presented in figure 3.2.

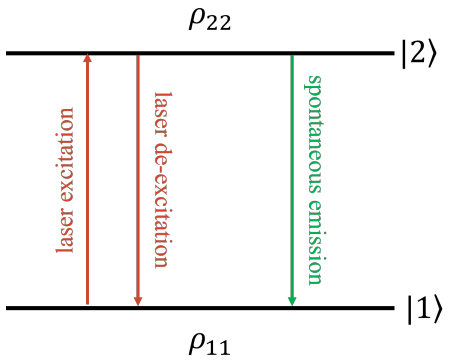

Figure 3.2: Diagram of a two-level system with spontaneous emission and identification of the ρ_{11} and ρ_{22} populations, as modeled by the Bloch equations (3.32).

The rate of spontaneous emission, Γ_{sp}, can be included in the Bloch equations by changing equation (3.5) to [41]

$$i\hbar\frac{dC_2}{dt} = \langle 2|\hat{\boldsymbol{H}}_I|2\rangle C_2 + \exp(i\omega_r t)\langle 2|\hat{\boldsymbol{H}}_I|1\rangle C_1 - i\hbar\frac{\Gamma_{sp}}{2}C_2\,. \tag{3.29}$$

This change is equivalent to the substitution [42]

$$\frac{\mathrm{d}C_2}{\mathrm{d}t} \to \left(\frac{\mathrm{d}}{\mathrm{d}t} + \frac{\Gamma_{sp}}{2}\right)C_2\,, \tag{3.30}$$

which takes into account that the probability of a bound particle staying in the excited energy level should decay. With use of the definitions (3.10) and (3.11), this leads to

$$\frac{\mathrm{d}\rho_{22}}{\mathrm{d}t} \to \left(\frac{\mathrm{d}}{\mathrm{d}t} + \Gamma_{sp}\right)\rho_{22} \qquad , \qquad \frac{\mathrm{d}\rho_{12}}{\mathrm{d}t} \to \left(\frac{\mathrm{d}}{\mathrm{d}t} + \frac{\Gamma_{sp}}{2}\right)\rho_{12}\,. \tag{3.31}$$

With the substitutions (3.31) the Bloch equations with spontaneous broadening are derived as

$$\begin{aligned}
\frac{\mathrm{d}\rho_{11}}{\mathrm{d}t} &= -\frac{\mathrm{d}\rho_{22}}{\mathrm{d}t} = \frac{i}{2}\mathcal{V}(\rho_{12} - \rho_{21}) + \Gamma_{sp}\rho_{22}\,, \\
\frac{\mathrm{d}\rho_{12}}{\mathrm{d}t} &= \frac{\mathrm{d}\rho_{21}^*}{\mathrm{d}t} = \frac{i}{2}\mathcal{V}^*(\rho_{11} - \rho_{22}) + \left(i\Delta - \frac{\Gamma_{sp}}{2}\right)\rho_{12}\,.
\end{aligned} \tag{3.32}$$

The spontaneous decay rate in equations (3.32) acts as a damping factor to the oscillations in the time evolution of the populations, which now tend towards a steady state, as represented in figure 3.3.

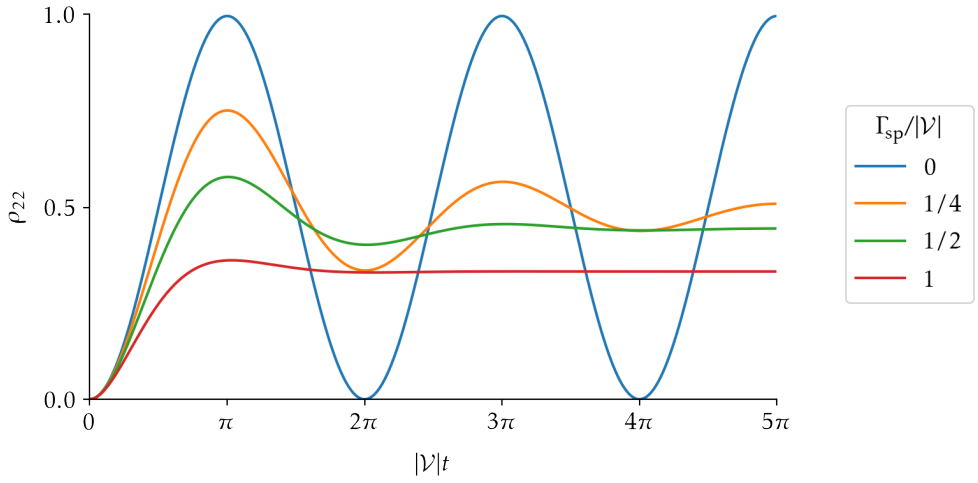

Figure 3.3: Time evolution of the ρ_{22} population with spontaneous emission for $\Delta = 0$ and different values of the broadening ratio $\Gamma_{sp}/|\mathcal{V}|$.

The steady-state population of the excited state can be obtained by setting the derivatives of equation (3.32) equal to zero, giving

$$\rho_{22}(\infty) = \frac{(|\mathcal{V}|/2)^2}{\Delta^2 + \left(\Gamma_{sp}/2\right)^2 + |\mathcal{V}|^2/2}\,. \tag{3.33}$$

It is possible to see, from equation (3.33), that the steady-state population is described by a Lorentzian curve with a full width at half maximum (FWHM) of

$$\mathrm{FWHM}_{\Gamma_{sp}} = \sqrt{\Gamma_{sp}^2 + 2|\mathcal{V}|^2}\,, \tag{3.34}$$

where the contributions of Γ_{sp} and $|\mathcal{V}|$ to the width of the steady-state curve are known as *radiative* and *power broadening*, respectively.

Equation (3.33) also shows that a saturation value of 1/2 is reached in the ideal case of $|\mathcal{V}| \gg \Delta, \Gamma_{sp}$. Figure 3.4 shows the dependence of the steady-state population upon the ratios $\Delta/|\mathcal{V}|$ and $\Gamma_{sp}/|\mathcal{V}|$.

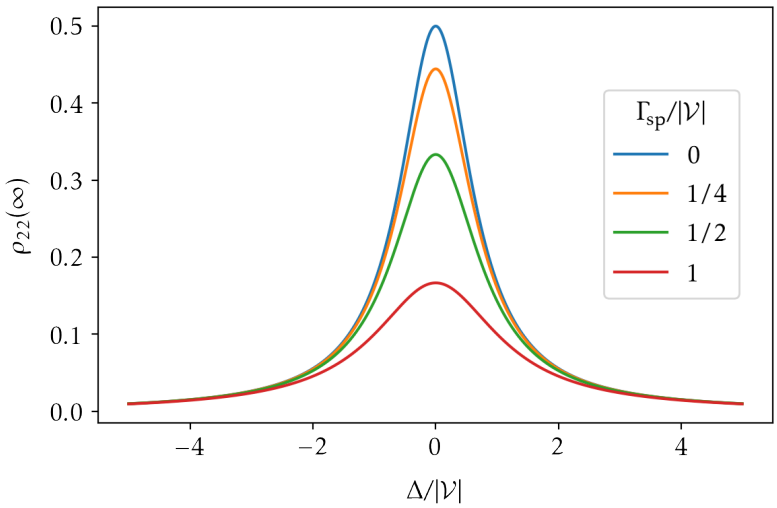

Figure 3.4: Steady-state population for different values of the broadening ratio $\Gamma_{sp}/|\mathcal{V}|$.

3.2.2 Collision broadening

Atoms in a gas are in constant interaction with each other via collisions. Two types of collision are possible, *elastic* and *inelastic*, with distinct effects on the time evolution of the populations.

3.2.2.1 Elastic collisions

In the event of an elastic collision, the atoms remain in the same energy levels and the effect of this type of collision on the energy level populations is reflected only by a phase change in the atomic wavefunctions [41]. This change in phase is represented by a decay rate, Γ_{el}, included in the time evolution of the coherence terms as

$$\frac{\mathrm{d}\rho_{12}}{\mathrm{d}t} = \frac{\mathrm{d}\rho_{21}^*}{\mathrm{d}t} = \frac{i}{2}\mathcal{V}^*(\rho_{11} - \rho_{22}) + \left(i\Delta - \frac{\Gamma_{sp} + \Gamma_{el}}{2}\right)\rho_{12}\,, \tag{3.35}$$

which acts as damping factor to the oscillations by increasing the decoherence between the energy level populations. Figure 3.5 shows the populations obtained from the Bloch

equations with elastic collision broadening, for the case of resonant excitation with no spontaneous broadening, i.e. $\Delta = 0$ and $\Gamma_{sp} = 0$. It is possible to see that in this particular case, the elastic collision rate simply dampens the population oscillations, with no change in the steady-state populations.

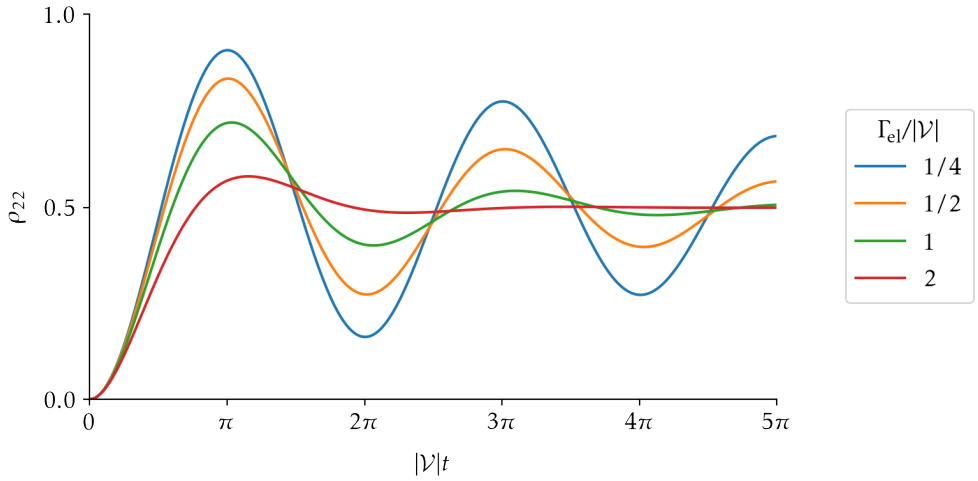

Figure 3.5: Time evolution of the ρ_{22} population with elastic collisions for $\Delta = 0$, $\Gamma_{sp} = 0$ and different values of the broadening ratio $\Gamma_{el}/|\mathcal{V}|$.

With the addition of the term Γ_{el}, the steady-state population of equation (3.33) becomes

$$\rho_{22}(\infty) = \frac{|\mathcal{V}|^2}{2|\mathcal{V}|^2 + 4\Delta^2 \frac{\Gamma_{sp}}{\Gamma_{sp}+\Gamma_{el}} + \Gamma_{sp}(\Gamma_{sp}+\Gamma_{el})} , \tag{3.36}$$

with a FWHM of

$$\mathrm{FWHM}_{\Gamma_{sp,el}} = \sqrt{2|\mathcal{V}|^2 \left(\frac{\Gamma_{sp}+\Gamma_{el}}{\Gamma_{sp}}\right) + (\Gamma_{sp}+\Gamma_{el})^2} , \tag{3.37}$$

which in the limit case of $\Gamma_{el} = 0$ tends to expression (3.34), as expected.

3.2.2.2 Inelastic collisions - two-level system

When an inelastic collision occurs, there is a change in the energy levels of the atoms. This effect is similar to that of spontaneous emission, as represented in figure 3.6, and can be introduced in the Bloch equations by a substitution analogous to (3.31). With the inclusion of the inelastic collision rate, Γ_{inel}, the substitution becomes

$$\frac{d\rho_{22}}{dt} \to \left(\frac{d}{dt} + \Gamma_{sp} + \Gamma_{inel}\right)\rho_{12} \quad , \quad \frac{d\rho_{12}}{dt} \to \left(\frac{d}{dt} + \frac{\Gamma_{sp}+\Gamma_{inel}}{2}\right)\rho_{22} , \tag{3.38}$$

and the Bloch equations (3.32) are transformed into

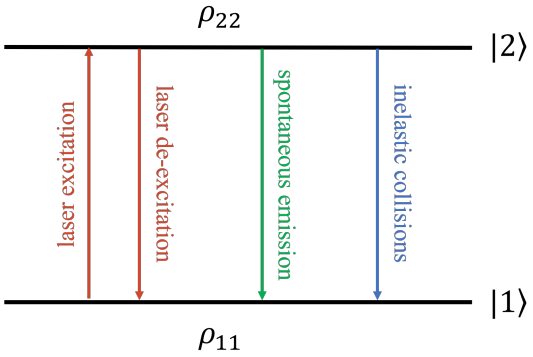

Figure 3.6: Diagram of a two-level system with spontaneous emission and inelastic collisions. The identified ρ_{11} and ρ_{22} populations are modeled by the Bloch equations (3.39).

$$\begin{aligned}\frac{\mathrm{d}\rho_{11}}{\mathrm{d}t} &= -\frac{\mathrm{d}\rho_{22}}{\mathrm{d}t} = \frac{i}{2}\mathcal{V}(\rho_{12}-\rho_{21}) + (\Gamma_{\mathrm{sp}}+\Gamma_{\mathrm{inel}})\rho_{22}\,,\\ \frac{\mathrm{d}\rho_{12}}{\mathrm{d}t} &= \frac{\mathrm{d}\rho_{21}^{*}}{\mathrm{d}t} = \frac{i}{2}\mathcal{V}^{*}(\rho_{11}-\rho_{22}) + \left(i\Delta - \frac{\Gamma_c}{2}\right)\rho_{12}\,,\end{aligned} \tag{3.39}$$

where Γ_c is the decay rate of the coherence terms, or *decoherence rate* [33], given by

$$\Gamma_c = \Gamma_{\mathrm{sp}} + \Gamma_{\mathrm{inel}} + \Gamma_{\mathrm{el}}\,. \tag{3.40}$$

The populations obtained from the collision-broadened Bloch equations (3.39) are similar to those obtained from the Bloch equations with spontaneous broadening (3.32), represented in figure 3.3, with increased damping from the contributions of the elastic and inelastic collision rates to the decoherence rate.

Contrary to the case of elastic collisions, the inelastic collision rate does contribute toward the steady-state population values as this rate has similar effects to those of spontaneous emission. The steady-state population of the excited level, obtained from the collision-broadened Bloch equations (3.39) is given by

$$\rho_{22}(\infty) = \frac{|\mathcal{V}|^2}{2|\mathcal{V}|^2 + 4\Delta^2\frac{\Gamma_{\mathrm{sp}}+\Gamma_{\mathrm{inel}}}{\Gamma_c} + (\Gamma_{\mathrm{sp}}+\Gamma_{\mathrm{inel}})\Gamma_c}\,. \tag{3.41}$$

3.2.2.3 Inelastic collisions - dark state

In the case of the quenching transition of equation (2.15), even though the final state represents the $1S(F=0)$ energy level, the total energy of the atom is different from that of the $1S(F=0)$ state before laser excitation, given the increase in kinetic energy. This new state can be represented by a third level [33], only accessible through inelastic collisions of the μp atoms in the $1S(F=1)$ level with the H_2 gas molecules, as represented in figure 3.7.

The added third state, with population ρ_{33}, is considered to be a *dark state*, that is, a state that is both unaffected and unreachable by laser excitation, given its low transition

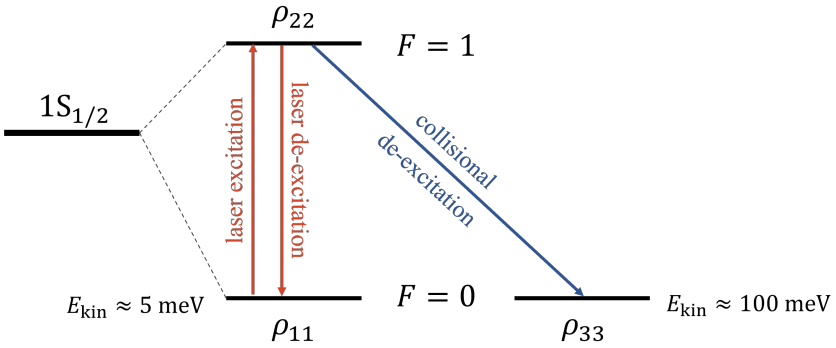

Figure 3.7: Representation of the ground-state HFS of μp as a three-level system with collisional de-excitation as modeled by the Bloch equations (3.42). Adapted from [33].

probability caused by the Doppler shift associated to its increased kinetic energy. The Bloch equations for a three-level system with a collisional dark-state are written as

$$\begin{aligned}
\frac{d\rho_{11}}{dt} &= \frac{i}{2}\mathcal{V}(\rho_{12} - \rho_{21}) + \Gamma_{sp}\rho_{22} \,, \\
\frac{d\rho_{12}}{dt} &= \frac{d\rho_{21}^*}{dt} = \frac{i}{2}\mathcal{V}^*(\rho_{11} - \rho_{22}) + \left(i\Delta - \frac{\Gamma_c}{2}\right)\rho_{12} \,, \\
\frac{d\rho_{22}}{dt} &= -\frac{d\rho_{11}}{dt} - \Gamma_{inel}\rho_{22} \,, \\
\frac{d\rho_{33}}{dt} &= \Gamma_{inel}\rho_{22} \,,
\end{aligned} \tag{3.42}$$

A three-level system with a time evolution governed by the Bloch equations (3.42) and a continuous electric field given by equation (2.9) will always tend towards the steady state $\rho_{11} = \rho_{22} = 0$ and $\rho_{33} = 1$ as $t \to \infty$. However, different values of the decoherence ratio $\Gamma_c/|\mathcal{V}|$ will alter the rate of population transfer between ρ_{11} and ρ_{22}, due to laser excitation/de-excitation, and between ρ_{22} and ρ_{33}, due to inelastic collisions. To illustrate the effects of the decoherence rate on the time evolution of the three-level system figure 3.8 shows the populations obtained from the Bloch equations (3.42) for different values of this ratio.

As can be seen in figure 3.8, the decoherence ratio greatly influences the rates of population transfer. In particular, it is seen that for low values of this ratio, i.e when $\Gamma_c \ll |\mathcal{V}|$, the population of the laser excited level (ρ_{22}) experiences Rabi oscillations similar to those obtained from the unbroadened Bloch equations (3.19), represented in figure 3.1. These oscillations, caused by a fast population transfer rate between ρ_{11} and ρ_{22}, lead to a slow and slightly oscillatory growth of the ρ_{33} population. In contrast, for higher values of the decoherence ratio, when $\Gamma_c \geq |\mathcal{V}|$, it is seen that the ρ_{22} population no longer oscillates but now quickly reaches a low (almost constant) value. In this regime, the quenched level population quickly rises towards its steady state, given the fast transfer

rate between the ρ_{22} and ρ_{33} populations. This, aligned with the low transfer rate of laser excitation/de-excitation, when $\Gamma_c > |\mathcal{V}|$, leads the system to behave as if the population transfer happened directly from ρ_{11} to ρ_{33}.

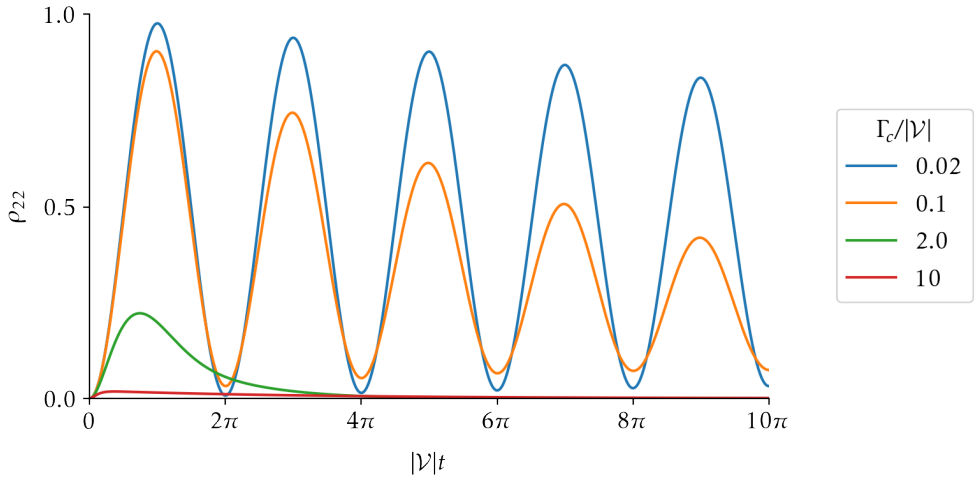

(a) Excited level population

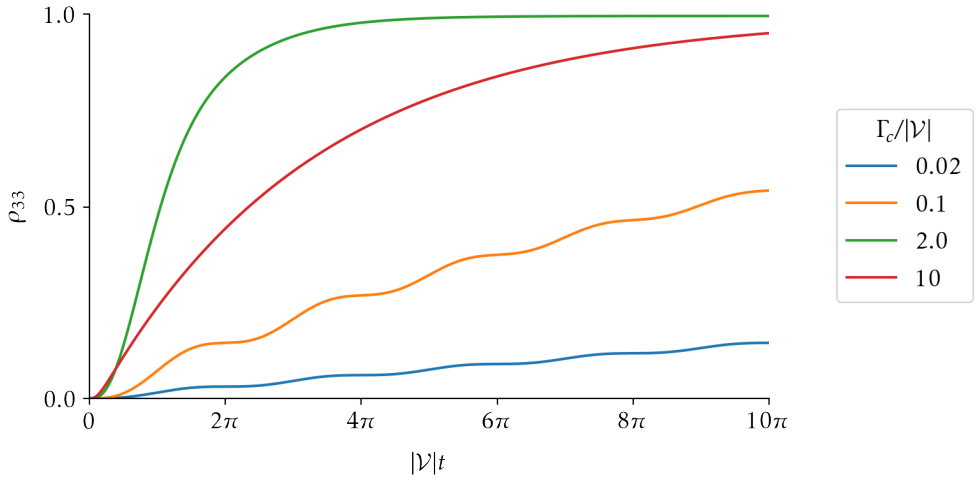

(b) Quenched level population ()

Figure 3.8: Time evolution of the ρ_{22} and ρ_{33} populations for different values of the decoherence ratio $\Gamma_c/|\mathcal{V}|$.

The two complementary regimes of population transfer here described are discussed in further detail in section 3.4 for time-limited electric fields of different intensities.

3.2.2.4 Collision rates in the HyperMu experiment

In the experimental setup described in section 2.2 the thermalized μp atoms are in constant collision with the H_2 gas molecules. These collisions can be modeled by collisional

rates, which can afterwards be included in the Bloch equations to obtain the collision-broadened populations, as previously shown. In particular, we are interested in the rates of elastic collisions for the μp atoms in the singlet and triplet states (Γ_{el}) and the inelastic collision rate of the μp atoms in the triplet state (Γ_{inel}), which are related to the following processes:

$$\Gamma_{\text{inel}} : \mu\text{p}^{F=1} + \text{H}_2 \longrightarrow \mu\text{p}^{F=0} + \text{H}_2 \tag{3.43}$$

$$\Gamma_{\text{el}} : \begin{cases} \mu\text{p}^{F=0} + \text{H}_2 & \longrightarrow \mu\text{p}^{F=0} + \text{H}_2 \\ & + \\ \mu\text{p}^{F=1} + \text{H}_2 & \longrightarrow \mu\text{p}^{F=1} + \text{H}_2 \ , \end{cases} \tag{3.44}$$

where the rate of elastic collisions is considered as the sum of the rates of both processes of equation (3.44). The obtained rates of elastic and inelastic collisions for these processes are presented in table 3.1 for the temperatures of 22 K and 50 K.

For a given process, the average collision rate of μp atoms in H_2 gas is given by [33]

$$\Gamma = \overline{v_r \sigma(v_r)} \rho_{\text{H}_2} \ , \tag{3.45}$$

where v_r is the relative velocity between the μp atoms and H_2 molecules, $\sigma(v_r)$ is the velocity- and spin-dependent cross section of the process and ρ_{H_2} is the number density of the H_2 gas in molecules per unit volume. The overline in the term $\overline{v_r \sigma(v_r)}$ denotes an average over the velocity and rotational level distribution of the H_2 molecules.

The average rates where calculated from the collision rates already averaged over the H_2 velocity and rotational level distributions, provided by Prof. Andrzej Adamczak, following the procedure in [43]. In this work the rates were afterwards averaged over the velocity distribution of μp atoms. It was assumed that the μp atoms behave as ideal gas particles, with their velocities following the Maxwell-Boltzmann distribution [44]

$$f(v)\,\mathrm{d}v = \sqrt{\frac{2}{\pi}} \left(\frac{m_{\mu p}}{k_B T} \right)^{3/2} v^2 \exp\left(-\frac{m_{\mu p} v^2}{2 k_B T} \right) \mathrm{d}v \ , \tag{3.46}$$

where $m_{\mu\text{p}}$ is the mass of the μp atom and k_B stands for the Boltzmann constant.

The distribution over the H_2 rotational levels is temperature dependent. As so, the average rates of table 3.1 where obtained from two sets of rates, each averaged over a different rotational level distribution. The two distributions considered are the Boltzmann and statistical distributions. At room temperature ($\sim$ 300 K) both distributions are similar with 75% ortho-hydrogen (odd rotational number) and 25% para-hydrogen (even rotational number). At lower temperatures, however, the statistical distribution deviates significantly from the Boltzmann distribution, e.g. at 22 K the Boltzmann distribution has

practically all molecules in the ground rotational level while the statistical distribution maintains 75% of the H_2 molecules in the first excited rotational level, which better models the gas after a fast cooling process where the Boltzmann distribution is only reached after a long time, given the slow transfer rate from the first excited rotational level to the ground rotational level (about 2% per week) [33].

Table 3.1: Collisional rates in MHz for μp atoms and H_2 gas molecules at different pressures and temperatures for Boltzmann and statistical H_2 rotational level distributions.

Collisional rates [MHz]

	$T = 22$ K		$T = 50$ K	
$P = 0.5$ bar	stat.	Boltz.	stat.	Boltz.
Γ_{el}	72	49	37	27
Γ_{inel}	82	93	34	37
$P = 1$ bar	stat.	Boltz.	stat.	Boltz.
Γ_{el}	144	98	74	56
Γ_{inel}	164	187	68	74
$P = 2$ bar	stat.	Boltz.	stat.	Boltz.
Γ_{el}	287	197	148	111
Γ_{inel}	328	374	137	148

3.2.3 Doppler broadening

This type of broadening occurs from the velocity distribution of the μp atoms, which, via the Doppler effect, leads to a shift in the frequencies at which they absorb or emit light [41].

For an electromagnetic wave propagating with velocity c, a particle moving with non-relativistic velocity v_x, in the direction of propagation of the wave, experiences a laser frequency in the laboratory frame of reference given by [41]

$$\omega' = \omega\left(1 + \frac{v_x}{c}\right), \tag{3.47}$$

relative to the emitted laser frequency ω. The experienced frequency ω' is then related to the laser frequency ω by the Doppler shift

$$\delta = \omega' - \omega = \omega\frac{v_x}{c}. \tag{3.48}$$

Assuming that the μp atoms follow an ideal gas behavior, the velocity component v_x is given by the one-dimensional Maxwell-Boltzmann velocity distribution [44]

$$f(v_x)\mathrm{d}v_x = \left(\frac{m_{\mu\mathrm{p}}}{2\pi k_\mathrm{B} T}\right)^{1/2} \exp\left(-\frac{m_{\mu\mathrm{p}} v_x^2}{2k_\mathrm{B} T}\right)\mathrm{d}v_x, \tag{3.49}$$

where $f(v_x)\mathrm{d}v_x$ represents the probability of a μp having a velocity component v_x in the range $[v_x, v_x + \mathrm{d}v_x]$ for a gas temperature T.

By combining equations (3.48) and (3.49) we obtain the distribution of Doppler frequency shifts [41]

$$f(\delta)\mathrm{d}\delta = \left(\frac{m_{\mu\mathrm{p}}c^2}{2\pi k_\mathrm{B}T\omega^2}\right)^{1/2}\exp\left(-\frac{m_{\mu\mathrm{p}}c^2}{2k_\mathrm{B}T\omega^2}\delta^2\right)\mathrm{d}\delta\,, \tag{3.50}$$

which gives the probability of a μp atom to experience a frequency shift between δ and $\delta + \mathrm{d}\delta$, for a given laser frequency ω, at a temperature T. The distribution of (3.50) is equivalent to the Gaussian distribution

$$f(\delta)\mathrm{d}\delta = \frac{1}{\Gamma_D\sqrt{2\pi}}\exp\left(-\frac{\delta^2}{2\Gamma_D^2}\right)\mathrm{d}\delta\,. \tag{3.51}$$

with a width Γ_D given by

$$\Gamma_D = \omega\sqrt{\frac{k_\mathrm{B}T}{m_{\mu\mathrm{p}}c^2}}\,, \tag{3.52}$$

which for the resonance frequency $\omega_r = 44.3$ THz of the ground state HFS transition in μp simplifies to

$$\Gamma_D \approx 12.7\sqrt{T}\ [\mathrm{MHz}], \tag{3.53}$$

where $[T]$ is in K.

The standard way of applying the frequency shift distribution of equation (3.51) to the populations obtained via the Bloch equations is through the linear convolution [41, 42]

$$\rho_{\mathrm{Doppler}}(t,\Delta) = (\rho * f)(t,\Delta) = \int_{-\infty}^{+\infty}\rho(t,\Delta-\delta)f(\delta)\mathrm{d}\delta\,. \tag{3.54}$$

This integration, here referred to as the *convolution method*, allows the Doppler-broadened populations to be calculated from the time and frequency detune dependent populations $\rho(t,\Delta)$, obtained from the Bloch equations. It is particular useful when dealing with constant amplitude fields, from which the expression for $\rho(t,\Delta)$ can be obtained analytically or through fast numerical integration of the Bloch equations, i.e. for the Bloch equations defined in (3.32) with an electric field given by expression (2.9) the Doppler-broadened steady-state population of the $1S(F=1)$ state obtained with the convolution method of equation (3.54) is given by the Voigt profile [41]

$$\rho_{22_{\mathrm{Doppler}}}(\infty) = \frac{1}{\Gamma_D\sqrt{2\pi}}\,\mathfrak{Re}\left[w\left(\frac{\Delta+ih}{\Gamma_D\sqrt{2}}\right)\right]\,, \tag{3.55}$$

where h stands for $\mathrm{FWHM}_{\Gamma_{\mathrm{sp}}}/2$ and $\mathfrak{Re}\,[w]$ stands for the real part of the Faddeeva error function. Figure 3.9 shows the difference between the Lorentzian profile of the steady-state population with no Doppler broadening ($\Gamma_D/|\mathcal{V}| = 0$), given by equation (3.33), and the Doppler-broadened Voigt profiles of equation (3.55).

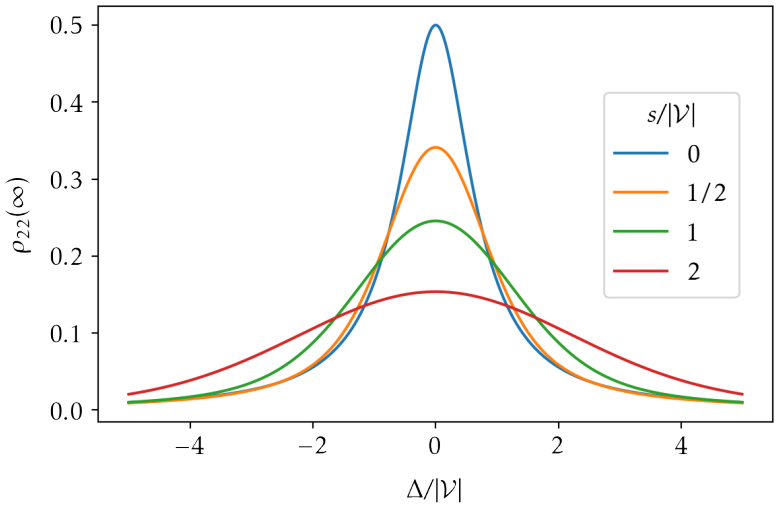

Figure 3.9: Doppler-broadened steady-state population values in function of the ratio $\Delta/|\mathcal{V}|$ for different values of the Doppler broadening ratio $\Gamma_D/|\mathcal{V}|$, with $\Gamma_{sp} = \Gamma_{el} = \Gamma_{inel} = 0$.

The convolution method of equation (3.54) has also been previously used to calculate the Doppler-broadened populations of the $1S(F = 0)$ and $1S(F = 1)$ energy levels of μp for laser pulses of constant intensity and various time durations [33]. In this present work, however, we aim to obtain the Doppler-broadened populations of the singlet and triplet ground state HFS energy levels of μp for a modeled electric field representing the laser pulse reflections inside the laser cavity of figure 2.3. This electric field introduces a random behavior into the Bloch equations and significantly complicates the process of obtaining a numerical expression for $\rho(t, \Delta)$ (see section 3.3).

3.2.4 Comparison of broadening effects in the HyperMu experiment

The Doppler width of equation (3.52) along with the decoherence, inelastic collision and spontaneous emission rates are the main broadening mechanisms for the steady-state populations obtained from the Bloch equations (3.42). In order to compare the relative contribution of each of these effects table 3.2 summarizes the broadening rates obtained for several conditions of temperature and pressure.

As can be seen from the results of table 3.2, for the considered experimental conditions, the spontaneous emission rate for the ground state HFS transition in μp represents a minor contribution to the broadening of the energy level populations, i.e. $\Gamma_{sp} \ll \Gamma_c, \Gamma_D$. As such, the spontaneous emission rate and it's related effect on the Bloch equations were neglected in all further stages of this work.

Table 3.2: Doppler width and decoherence and spontaneous emission rates at various conditions of temperature and pressure. The spontaneous emission rate, Γ_{sp}, refers to the $1S(F=1) \longrightarrow 2S(F=0)$ transition in μp and it's value was taken from [33]. Collision rates taken from table 3.1 assuming a statistical distribution for the H_2 rotational levels.

T [K]	P [bar]	Γ_{sp} [MHz]	Γ_c [MHz]	Γ_D [MHz]
22	0.5	1.96×10^{-12}	154	60
22	1		308	60
22	2		615	60
50	0.5		71	90
50	1		142	90
50	2		285	90

3.3 Effective Laser Field

The theoretical formalism presented so far was developed under the consideration of a constant amplitude electric field. However, the laser field inside the cavity is expected to suddenly increase and then decay exponentially as the laser pulse is reflected back and forth. Therefore, to correctly model the behavior of the μp energy level populations within the experimental setup presented in section 2.2, an accurate description of the electromagnetic field inside the laser cavity is required.

In this section we introduce a model for the electric field based on successive reflections of the laser pulse inside the cavity of figure 2.3. In order to avoid the increased complexity in the calculation of $\rho(t, \Delta)$, caused by the random nature of the modeled electric field, we present also an alternative method of obtaining the Doppler-broadened populations from the Bloch equations.

3.3.1 Initial description

The laser's electromagnetic field consists of an initial pulse at a frequency ω that is folded within a toroidal cavity by reflecting at the mirror surface. The toroidal cavity has a mirror surface with a given reflectivity R and a diameter D.

Upon reflection, the laser pulse is assumed to have decreased in amplitude by a factor of R as well as being shifted by a random phase ϕ. This random parameter attempts to model a very complicated behavior of the light inside the cavity in which the light reaching the atom is not phase correlated with the light before reflection, leading to a random interference pattern between the reflected pulses.

The electric field at the center of the cavity can be written as the incoherent sum of its initial and reflected pulses as [45]

$$E(t) = E_0 \sum_n^\infty R^n G_\tau(t - t_n) \cos(\omega t + \phi_n) \,, \tag{3.56}$$

where $G_\tau(t-t_n)$ is the Gaussian shape

$$G_\tau(t-t_n) = \left(\frac{1}{\tau\sqrt{\pi}}\right)^{1/2} \exp\left[-\frac{(t-t_n)^2}{2\tau^2}\right], \tag{3.57}$$

of center $t_n = n\frac{D}{c}$ and pulse duration τ. The pulses are normalized according to

$$\int_{-\infty}^{\infty} G_\tau^2(t)\,\mathrm{d}t = 1\ , \tag{3.58}$$

so that the fluence of the initial pulse is solely dependent on the field amplitude E_0 (see section 3.4).

Inputing the electric field of equation 3.56 into the Bloch equations would lead to the introduction of a random behavior in the obtained populations, due to the random phase ϕ_n attributed to each reflection. In order to deal with this behavior, the populations would need to be calculated for a set of electric fields with the same values of τ, R, D. Then, in order to obtain the Doppler-broadened populations through the convolution method, described in section 3.2.3, this process would have to be repeated for a range of frequency detuning (Δ) in order to obtain the values of $\rho(t,\Delta)$, which could then be used to calculate the Doppler convolution integral of equation (3.54). The described process is represented in the diagram of figure 3.10.

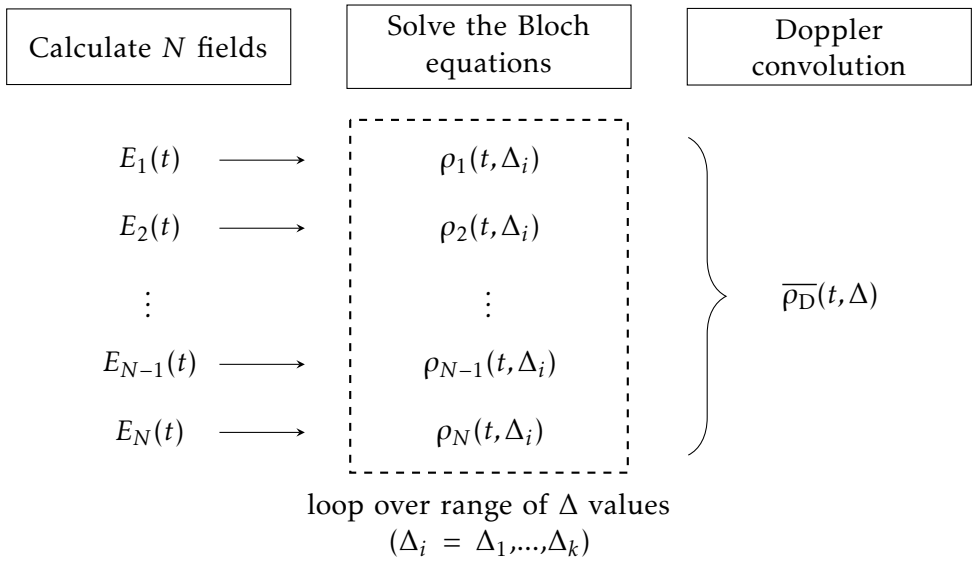

Figure 3.10: Diagram of the necessary process for calculating the average Doppler-broadened populations ($\overline{\rho_D}$) with the convolution method and the modeled electric field of equation (3.56). The subscripts with values of 1 through N are used for relating the calculated populations with their relative field and should not to be confused with the double index subscripts in ρ_{11}, ρ_{22}, etc. The large bracket represents the process of averaging over the N calculated populations, for each Δ_i, to obtain the average population $\overline{\rho}(t,\Delta)$, before performing the Doppler convolution.

The biggest disadvantage of this method lies in the fact that the convolution integral can only be calculated when the values of $\overline{\rho}(t,\Delta)$ are known. Therefore, even in the particular cases where we are only interested in determining the energy level populations for a specific detune value $\Delta = \Delta_0$ the loop over a range of Δ values, symbolized by the dashed box of figure 3.10, is unavoidable.

3.3.2 Doppler-shifted field

In order to avoid part of the increased complexity attributed to the convolution method, caused by the random nature of the modeled electric field, we present in this section an alternative method of obtaining the Doppler-broadened populations. This method, here referred to as the *Doppler shift method*, relies on the inclusion of the Doppler effect directly in the calculation of the electric field, by taking into account the frequency shift caused by the velocity of the μp atoms. In doing so, the obtained *Doppler-shifted electric field* can be included in the Bloch equations, from which the Doppler-broadened energy level populations can be obtained without the need of a convolution integral.

Considering that the μp atoms have a given velocity $\vec{v}$, the component (v_x) of this velocity in the direction of propagation of the electric field will cause a Doppler shift in the perceived frequency, as explained in section 3.2.3. If the electric field propagates in the x direction, as represented in figure 3.11, the Doppler-shifted frequency is given by equation (3.47) and the field of equation (3.56) becomes

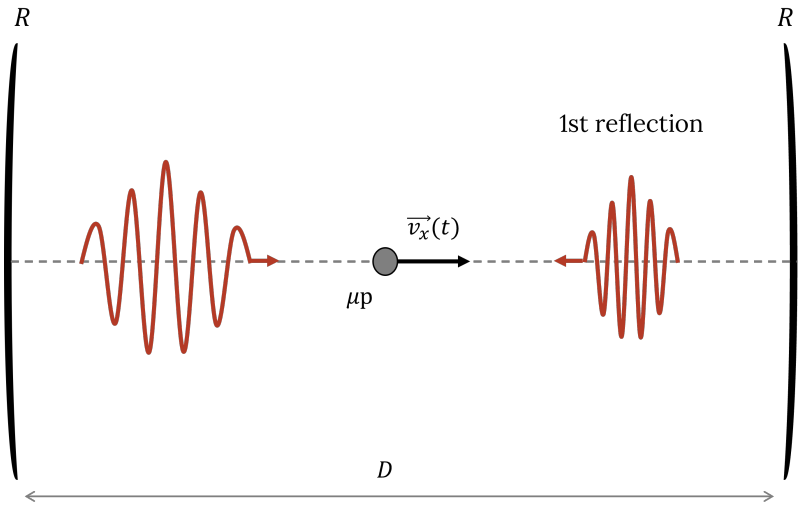

Figure 3.11: Representation of the first pulse and first reflection of the laser's Doppler-shifted electric field inside the laser cavity accounting for the velocity of the μp atoms.

$$E(t) = E_0 \sum_n^{\infty} R^n G_\tau(t - t_n) \cos\left[\left(\omega + \omega\frac{v_x}{c}\right)t + \phi_n\right], \tag{3.59}$$

which can also be written as the product of a fast oscillation of amplitude E_0 and frequency ω and a dimensionless Doppler-shifted oscillation ($\mathcal{E}$) with frequency $\omega\frac{v_x}{c}$

$$E(t) = \frac{E_0}{2} e^{i\omega t} \mathcal{E}(t) + \text{c.c} \ , \tag{3.60}$$

where

$$\mathcal{E}(t) = \sum_{n}^{\infty} R^n G_\tau (t - t_n) \exp\left(i\omega_D + i\phi_n\right) \ , \tag{3.61}$$

and ω_D is the Doppler shift frequency, given by

$$\omega_D = \omega \frac{v_x}{c} \ . \tag{3.62}$$

In order to derive the Bloch equations for the Doppler-shifted field of equation (3.59), we first define the time-dependent Rabi frequency

$$\mathcal{V}(t) = \frac{eE_0}{\hbar} \mathcal{M} \mathcal{E}^*(t) \ , \tag{3.63}$$

analogous to the previously defined Rabi frequency of equation (3.16) but with a time-dependent amplitude given by the modeled Doppler-shifted field. Then, with the use of the rotating-wave approximation introduced in section 3.1.1, we obtain the *Doppler-shifted Bloch equations*

$$\begin{aligned}
\frac{\mathrm{d}\rho_{11}}{\mathrm{d}t} &= \left[\frac{i}{2}\mathcal{V}(t)\rho_{12} + \text{c.c}\right] + \Gamma_{\text{sp}}\rho_{22} \\
\frac{\mathrm{d}\rho_{12}}{\mathrm{d}t} &= \frac{\mathrm{d}\rho_{21}^*}{\mathrm{d}t} = \frac{i}{2}\mathcal{V}^*(t)\left(\rho_{11} - \rho_{22}\right) + \left(i\Delta - \frac{\Gamma_c}{2}\right)\rho_{12} \\
\frac{\mathrm{d}\rho_{22}}{\mathrm{d}t} &= -\frac{\mathrm{d}\rho_{11}}{\mathrm{d}t} - \Gamma_{\text{inel}}\rho_{22} \\
\frac{\mathrm{d}\rho_{33}}{\mathrm{d}t} &= \Gamma_{\text{inel}}\rho_{22} \ ,
\end{aligned} \tag{3.64}$$

which model the time evolution of the ground state HFS energy level populations of μp for a Doppler-shifted electric field dependent on the laser and cavity parameters as well as the temperature and pressure conditions of the H_2 gas, which determine the velocity of the μp atoms.

With the Doppler-shifted Bloch equations (3.64) it its possible to obtain the Doppler-broadened energy level populations without the need of the convolution integral of equation (3.54), through the process represented in figure 3.12. In particular, the populations can know be obtained for a specific frequency detuning ($\Delta = \Delta_0$) without knowledge of the general population function $\rho(t, \Delta)$.

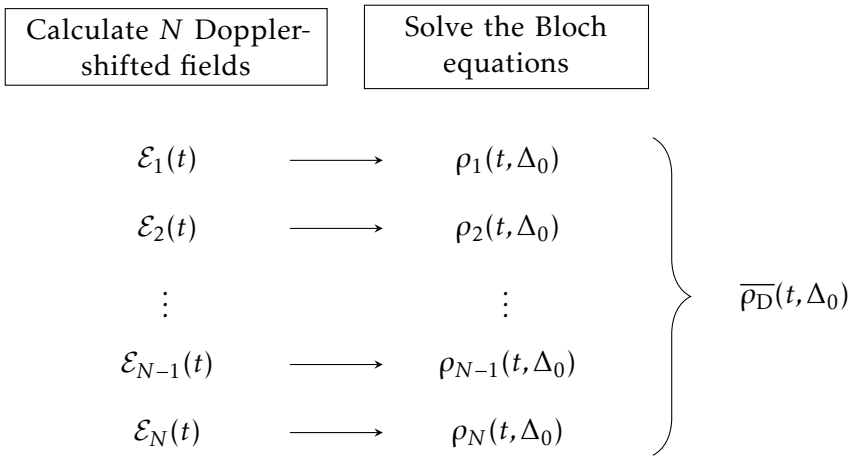

Figure 3.12: Diagram of the necessary process for calculating the average Doppler-broadened populations ($\overline{\rho_D}$) with the Doppler-shifted field of equation (3.59). The subscripts with values of 1 through N are used for relating the calculated populations with their relative field and should not to be confused with the double index subscripts in ρ_{11}, ρ_{22}, etc. The large bracket represents the process of averaging over the N calculated populations to obtain the average Doppler-broadened population $\overline{\rho_D}(t,\Delta_0)$ for a specific value of laser frequency detuning $\Delta = \Delta_0$.

3.4 Laser fluence

It is important that the electromagnetic field of the laser is defined in terms of experimentally controllable variables. Here we chose to define the electric field in relation to the laser fluence, a measure of the energy radiated per unit area, defined as the time integral of the laser intensity $\mathcal{I}$.

For a time period Δt the fluence is given by

$$\mathcal{F}_{\Delta t} = \int_{-\Delta t/2}^{\Delta t/2} \mathcal{I}(t)\,\mathrm{d}t = \varepsilon_0 c \int_{-\Delta t/2}^{\Delta t/2} E^2(t)\,\mathrm{d}t \quad [\mathrm{J/m^2}]\,, \tag{3.65}$$

where ε_0 is the vacuum permittivity. The total fluence ($\mathcal{F}$) of a laser pulse can then be obtained by extending the limits of integration of equation (3.65) to infinity, as

$$\mathcal{F} = \varepsilon_0 c \int_{-\infty}^{\infty} E^2(t)\,\mathrm{d}t\,. \tag{3.66}$$

3.4.1 Fluence of the Doppler-shifted field

For a field defined by equation (3.59) the total fluence is given by

$$\begin{aligned}\mathcal{F} &= \varepsilon_0 c \int_{-\infty}^{\infty} \left[E_0 \sum_n^{\infty} R^n G_\tau(t-t_n)\cos(\omega_D t+\phi_n)\right]^2 \mathrm{d}t \\ &= \varepsilon_0 c E_0^2 \int_{-\infty}^{\infty} \left[\sum_n^{\infty} R^{2n} G_\tau^2(t-t_n)\cos^2(\omega_D t+\phi_n) + \right. \\ &\quad \left. + \sum_{i\neq j}^{\infty} R^{i+j} G_\tau(t-t_i) G_\tau(t-t_j)\cos(\omega_D t+\phi_i)\cos(\omega_D t+\phi_j)\right] \mathrm{d}t \ ,\end{aligned} \tag{3.67}$$

where ω_D is the Doppler shifted frequency, defined in (3.62).

Considering that every emitted laser pulse produces a random electric field inside the cavity, caused by the random phases ϕ_n upon reflection, equation (3.67) states that for each of these random fields the total fluence is given by the sum of two terms. One, common to all fields with the same values of τ, R and D, given by

$$\begin{aligned}\mathcal{F}_{\text{com.}} &= \varepsilon_0 c E_0^2 \int_{-\infty}^{\infty} \sum_n^{\infty} R^{2n} G_\tau^2(t-t_n)\cos^2(\omega_D t+\phi_n)\,\mathrm{d}t \\ &= \varepsilon_0 c E_0^2 \left(\frac{1}{1-R^2}\right) \int_{-\infty}^{\infty} G_\tau^2(t)\cos^2(\omega_D t+\phi_n)\,\mathrm{d}t \\ &= \frac{\varepsilon_0 c E_0^2}{2}\left(\frac{1}{1-R^2}\right) ,\end{aligned} \tag{3.68}$$

under the condition $\omega_D \gg 2\pi/\tau$ and the normalization of equation (3.58). And an interference term

$$\mathcal{F}_{\text{int.}} = \varepsilon_0 c E_0^2 \int_{-\infty}^{\infty} \sum_{i\neq j}^{\infty} R^{i+j} G_\tau(t-t_i) G_\tau(t-t_j)\cos(\omega_D t+\phi_i)\cos(\omega_D t+\phi_j)\,\mathrm{d}t \ , \tag{3.69}$$

which depends upon the phase of each reflection and therefore cannot be further simplified. However it is possible to see that

$$\left| \int_{-\infty}^{\infty} G_\tau(t-t_i) G_\tau(t-t_j)\cos(\omega_D t+\phi_i)\cos(\omega_D t+\phi_j)\,\mathrm{d}t \right| \leq \int_{-\infty}^{\infty} G_\tau^2(t)\cos^2(\omega_D t)\,\mathrm{d}t \ , \tag{3.70}$$

which leads to

$$|\mathcal{F}_{\text{int.}}| \leq \mathcal{F}_{\text{com.}} \ . \tag{3.71}$$

With the initial laser pulse fluence $\mathcal{F}_0$, defined by

$$\mathcal{F}_0 = \varepsilon_0 c E_0^2 \int_{-\infty}^{\infty} G_\tau^2 \cos^2(\omega_D t)\,\mathrm{d}t = \frac{\varepsilon_0 c E_0^2}{2} \ , \tag{3.72}$$

and equations (3.67), (3.68) and (3.71) we reach the condition

$$0 \leq \mathcal{F} \leq \frac{2\mathcal{F}_0}{1-R^2} \,. \tag{3.73}$$

It is possible to see from equations (3.69) and (3.73) that $\mathcal{F} = 0$ happens for maximum destructive interference inside the cavity while $\mathcal{F} = 2\mathcal{F}_0/(1-R^2)$ is the fluence obtained for maximum constructive interference. Since all values of $\mathcal{F}$ in the interval between maximum destructive and constructive interference should follow a symmetric probability distribution around the halfway value of $\mathcal{F}_0/(1-R^2)$, it is then expected that for several electric fields, each generated by the same initial laser pulse of fluence $\mathcal{F}_0$, the average fluence inside the cavity is given by

$$\overline{\mathcal{F}} = \frac{\mathcal{F}_0}{1-R^2} \,, \tag{3.74}$$

where the overline represents an average over several electric fields with the same values of $\mathcal{F}_0$, τ and R.

3.4.2 Limiting regimes

With the use of equation (3.72) it is possible to obtain the time-dependent Rabi frequency in terms of the initial laser pulse fluence as

$$\mathcal{V}(t) = \frac{e\mathcal{M}}{\hbar}\sqrt{\frac{2\mathcal{F}_0}{\varepsilon_0 c}}\mathcal{E}(t) = \mathcal{V}_0\sqrt{\mathcal{F}_0}\mathcal{E}(t) \,, \tag{3.75}$$

where

$$\mathcal{V}_0 = \frac{e\mathcal{M}}{\hbar}\sqrt{\frac{2}{\varepsilon_0 c}} \tag{3.76}$$

is independent of time, fluence and pulse duration.

Considering the simple case of a single Gaussian pulse with no reflections, for which

$$\mathcal{E}(t) = G_\tau(t - t_0) \,, \tag{3.77}$$

and

$$\mathcal{F} = \mathcal{F}_0 \Longrightarrow \mathcal{V}(t) = \mathcal{V}_0\sqrt{\mathcal{F}}G_\tau(t - t_0) \,, \tag{3.78}$$

the three-level system Bloch equations (3.64) can be solved numerically in order to obtain the energy level populations for two different oscillation regimes (analogous to those of section 3.2.2.3), defined by the dimensionless ratio $\Gamma_c/\mathcal{V}_0^2\mathcal{F}$.

When $\Gamma_c \geq \mathcal{V}_0^2\mathcal{F}$, the rate of population transfer from ρ_{22} to ρ_{33} is close to or greater than the rate of transfer between ρ_{11} and ρ_{22}. In these conditions, assuming that $\rho_{11} = 1$ at $t = 0$, it is as if the population transfer happened directly from ρ_{11} to ρ_{33}, preventing any oscillations between ρ_{11} and ρ_{22} and leading the steady-state ρ_{33} population to quickly

reach a saturation value with the increase of laser pulse duration, as shown in figure 3.13(a).

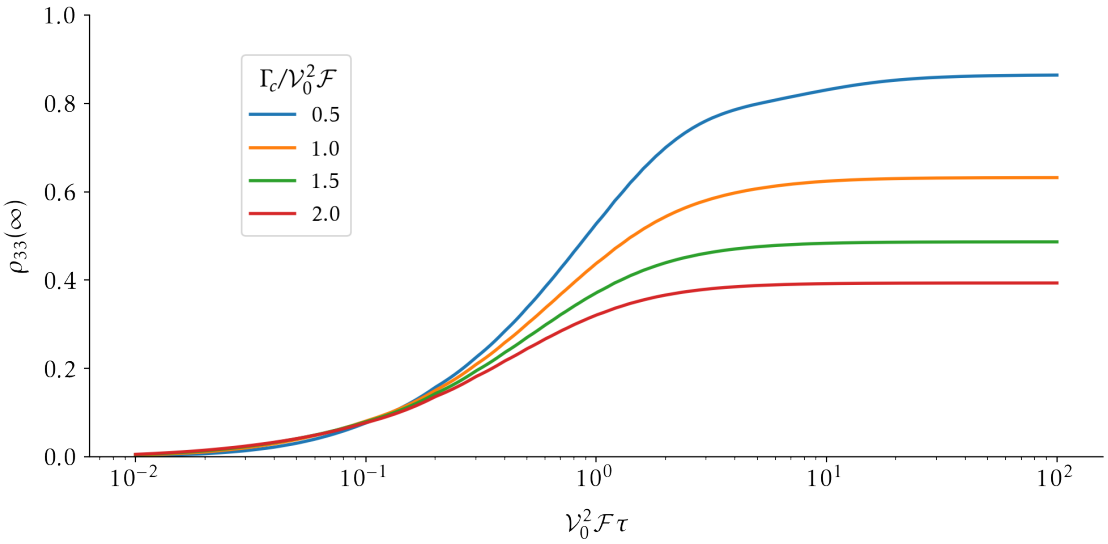

(a) $\Gamma_c \sim \mathcal{V}_0^2\mathcal{F}$

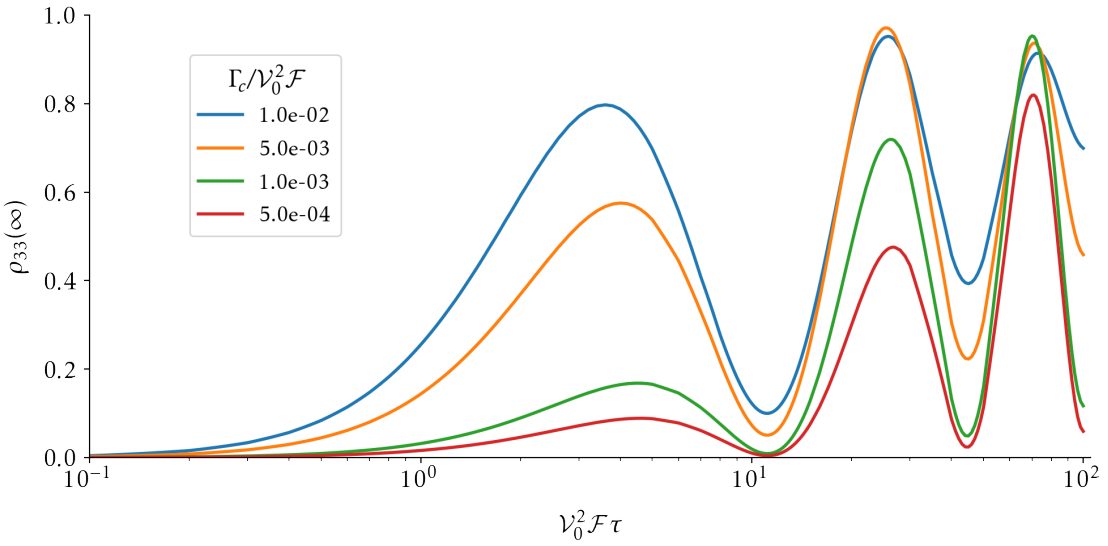

(b) $\Gamma_c \ll \mathcal{V}_0^2\mathcal{F}$

Figure 3.13: Steady-state ρ_{33} population *vs.* dimensionless laser pulse duration for two limiting regimes with different values of the broadening ratio $\Gamma_c/\mathcal{V}_0^2\mathcal{F}$, with $\Gamma_{\text{el}} = \Gamma_{\text{inel}}$ and $\Gamma_{\text{sp}} = 0$, such that $\Gamma_c = 2\Gamma_{\text{inel}}$. No Doppler broadening considered ($\Gamma_D = 0$).

It is important to note that Γ_c contains not only the inelastic collision ratio, representing the rate of transfer from ρ_{22} to ρ_{33}, but also the rate of elastic collision, which contributes to the damping of the oscillations between the ρ_{11} and ρ_{22} populations. It is this damping that leads to lower steady-state ρ_{33} populations for larger values of the ratio $\Gamma_c/\mathcal{V}_0^2\mathcal{F}$ in the results of figure 3.13(a).

In the case of $\Gamma_c \ll \mathcal{V}_0^2\mathcal{F}$, however, both the rate of population transfer from ρ_{22} to ρ_{33} and the damping of the oscillations between ρ_{11} and ρ_{22} become smaller. This leads the ρ_{11} and ρ_{22} populations to behave according to equations (3.27) and (3.28) preventing the saturation of the ρ_{33} population and causing it to oscillate with the increasing values of laser pulse duration, as shown in figure 3.13(b).

These two limiting regimes have been previously studied for rectangular laser pulses of constant intensity [33]. The low oscillation regime represented in figure 3.13(a), characterized by $\Gamma_c \geq \mathcal{V}_0^2\mathcal{F}$, produces steady-state populations that can be approximated by those obtained from Fermi's golden rule [41] and is therefore referred to as the *Fermi golden rule regime* [33]. In contrast, the regime with highly oscillatory behavior, represented in figure 3.13(b), is denoted as the *Rabi oscillation regime*.

4

Simulation

A simulation method was developed using Python [46] in order to study the populations obtained from the Bloch equations when considering the effective shape of the electric field inside the laser cavity, as explained in section 3.3, while also accounting for the broadening effects of section 3.2.

4.1 General structure

The simulation is divided into two main parts, represented by the left and right processes of figure 4.1.

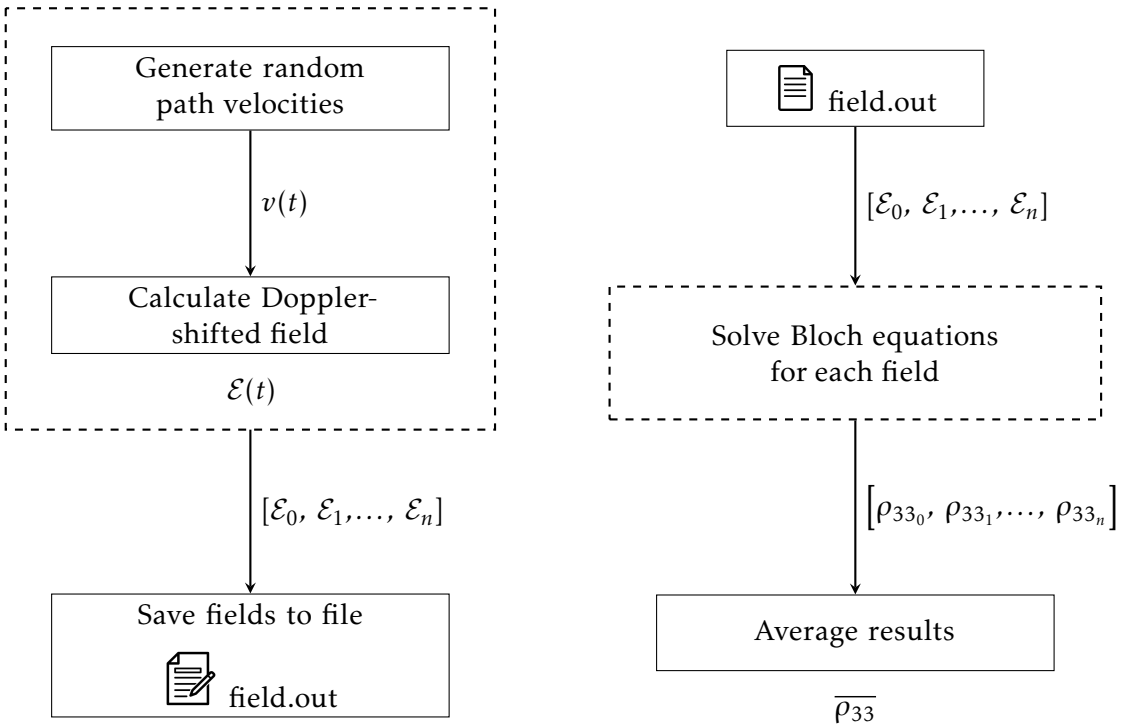

Figure 4.1: Diagram of the general structure of the simulation. Dashed boxes indicate processes or groups of processes which are run in a loop.

The first part consists on calculating Doppler-shifted fields, for given sets of experimental conditions. The Doppler-shifted fields are used in order to take advantage of the random nature of the electric field (due to the random phase upon reflection) by including the effects of Doppler broadening directly in the calculation of the electric fields via a Monte Carlo approach, following the procedure explained in section 4.3. The velocities used for the Doppler-shifted fields, explained in detail in section 4.2, are sampled from one-dimensional Maxwell-Boltzmann distributions (3.49) and follow a random path behavior.

The simulated fields are saved into files that are afterwards read and used to solve the Bloch equations for any given value of laser fluence. The Bloch equations are solved numerically using an implementation of the Runge-Kutta fourth-order method, discussed in section 4.4.

4.2 Particle motion

In order to calculate the Doppler-shifted field we first need to obtain the velocity function of the μp atoms. These atoms are assumed to behave as an ideal gas inside the laser cavity with their velocities following Maxwell-Boltzmann distributions.

To generate a velocity function we sample velocities from a Maxwell-Boltzmann distribution, with collisions (changes in velocity) following a Poisson distribution. The probability of collision at each time step $\mathrm{d}t$ is given by

$$p_{\mathrm{coll}} = \Gamma_{\mathrm{el}}\, \mathrm{d}t \tag{4.1}$$

At each time step a random number ($a \in [0,1]$) is generated and compared with p_{coll}. If $a < p_{\mathrm{coll}}$ a collision takes place and a new velocity is sampled from the Maxwell-Boltzmann distribution, otherwise the velocity remains unchanged. A simple version of this algorithm can be written in Python, as shown in listing A.3, provided that we build a function that returns a sampled 1-dimensional velocity from a Maxwell-Boltzmann distribution for particles of mass m at temperature T (see listing A.2). An example of sampled one-dimensional Maxwell-Boltzmann velocities is presented in figure 4.2.

To illustrate the Poisson sampling of collision times, figure 4.3 shows the sampled probability of observing N collisions in a time interval of $100/\Gamma_{\mathrm{el}}$ compared with the Poisson distribution [47]

$$P(X = N) = \frac{\lambda^N e^{-\lambda}}{N!} \tag{4.2}$$

where λ is the expected level of occurrences. In the case of a time interval of $100/\Gamma_{\mathrm{el}}$ it follows that $\lambda = 100$.

An example of a 2D random path with velocities and collision times generated with the algorithm of listing A.3 is shown in figure 4.4.

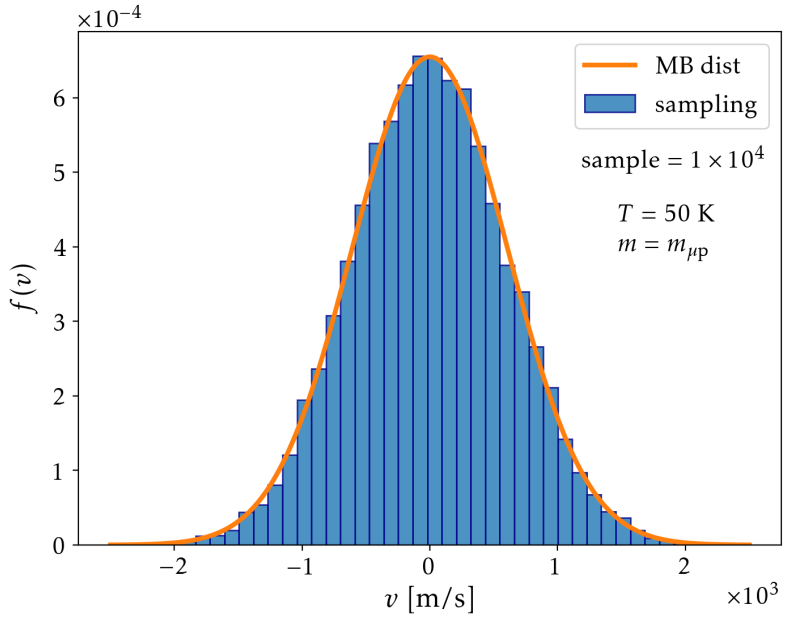

Figure 4.2: Sampled velocities from a Maxwell-Boltzmann distribution for μH atoms.

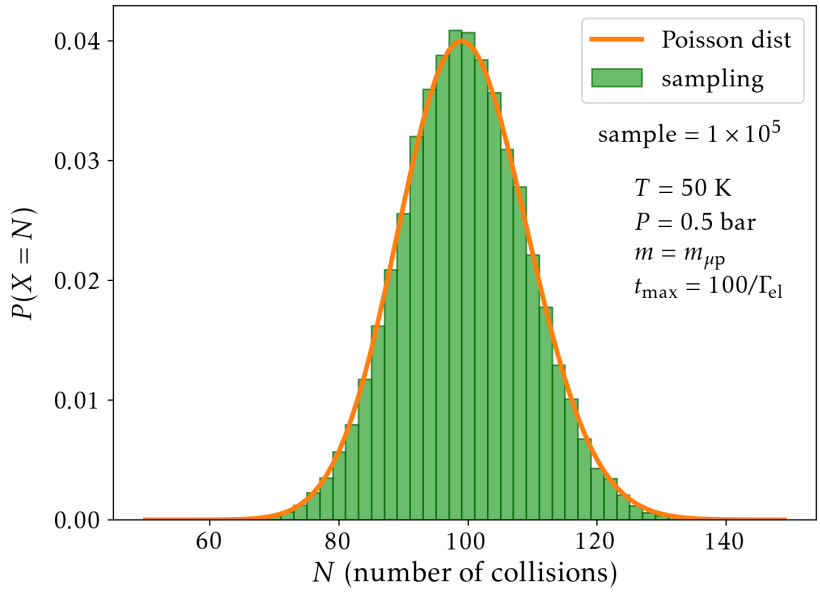

Figure 4.3: Sampled probability of the number of collisions observed for a time interval of $100/\Gamma_{\mathrm{el}}$.

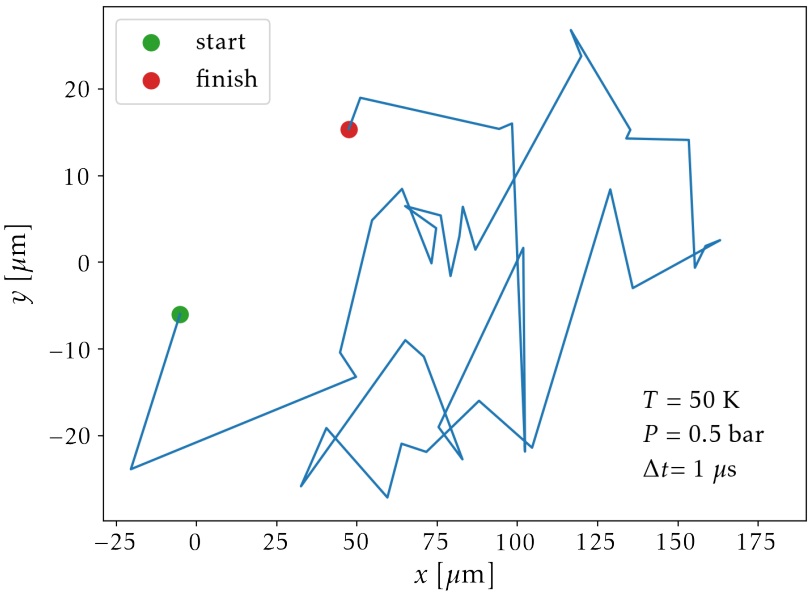

Figure 4.4: Simulated 2D random path for a μH atom in H_2.

4.3 Cavity field

To simulate the electric field inside the laser cavity we use the Doppler-shifted field of section 3.3.2 with Doppler-shifted frequencies calculated from the velocities obtained through the algorithm of listing A.3.

In order to account for the abrupt changes in the Doppler-shifted frequency, caused by the change in velocity at each collision, an algorithm was built to construct a continuous wave with abrupt changes in frequency. The wave is built from different frequency segments that are phase-shifted in order to avoid any possible discontinuities. Two wave segments with frequencies ω_1 and ω_2 and phases ϕ_1 and ϕ_2 intercepting at $t = t_0$ form a continuous wave if

$$\phi_1 = \phi_0 + (\omega_0 - \omega_1)t_0 \,, \tag{4.3}$$

as exemplified in figure 4.5.

With continuous waves of Doppler shift frequencies, given by

$$\omega_D(t) = \omega \frac{v(t)}{c} \,, \tag{4.4}$$

it is possible to compute the terms

$$\exp\left[i\omega_D(t) + i\phi_n\right] \,, \tag{4.5}$$

from the Doppler-shifted field of equation (3.61). The complete field can then be obtained by multiplying the n terms given by equation (4.5) with the reflected Gaussian pulses

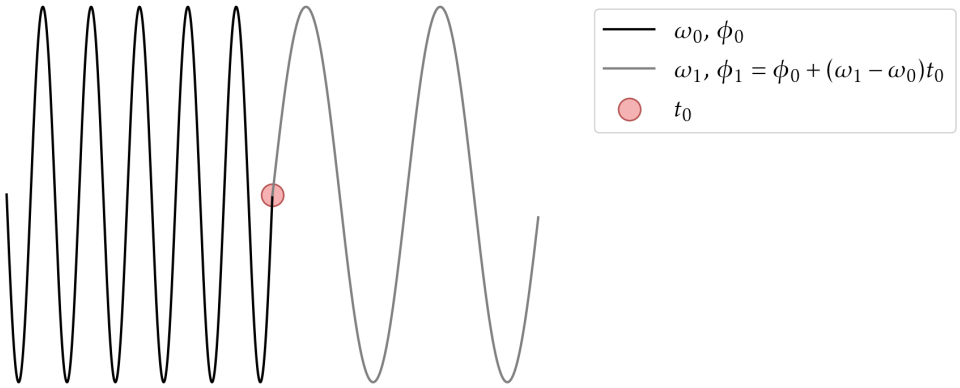

Figure 4.5: Continuous wave with different frequency segments intercepting at $t = t_0$.

$$R^n G_\tau(t - t_n) \,, \tag{4.6}$$

and summing all the resulting terms according to equation (3.61).

The summations presented in the model of section 3.3 have an infinite number of reflections (i.e. n ranges from 0 to ∞), in a simulation, however, a maximum value for n must be defined. In the developed simulation this value is calculated from an input minimum amplitude (`minAmp`, see listing A.5) as

$$n_{\max} = \frac{\ln(\text{minAmp})}{\ln(R)} \,. \tag{4.7}$$

In all the simulations performed in this work the value of 0.01 was chosen for `minAmp`, such that the last reflection considered represents 1% of the initial laser pulse amplitude.

From the value of $n_{\max}$ we also define the time interval to consider, since it is directly related to the last simulated reflection. However, since the time interval is also used for solving the Bloch equations, it is important that we take into account the possibility of population transfer due to inelastic collisions when no electric field is present. The time interval must therefore always be greater than the time of the last reflection $t_{n_{\max}}$.

A diagram of the simulation process for the cavity field is represented in figure 4.6, and corresponds to a detailed view of the dashed box on the left side of figure 4.1. The process is ran in a loop, as represented by the dashed box of figure 4.1, in order for the Bloch equations to be solved for an array of electric fields to then calculate the average populations for each set of experimental conditions. To illustrate the random nature of the electric field inside the laser cavity, figure 4.7(a) shows two Doppler-shifted fields generated for the same set of experimental conditions.

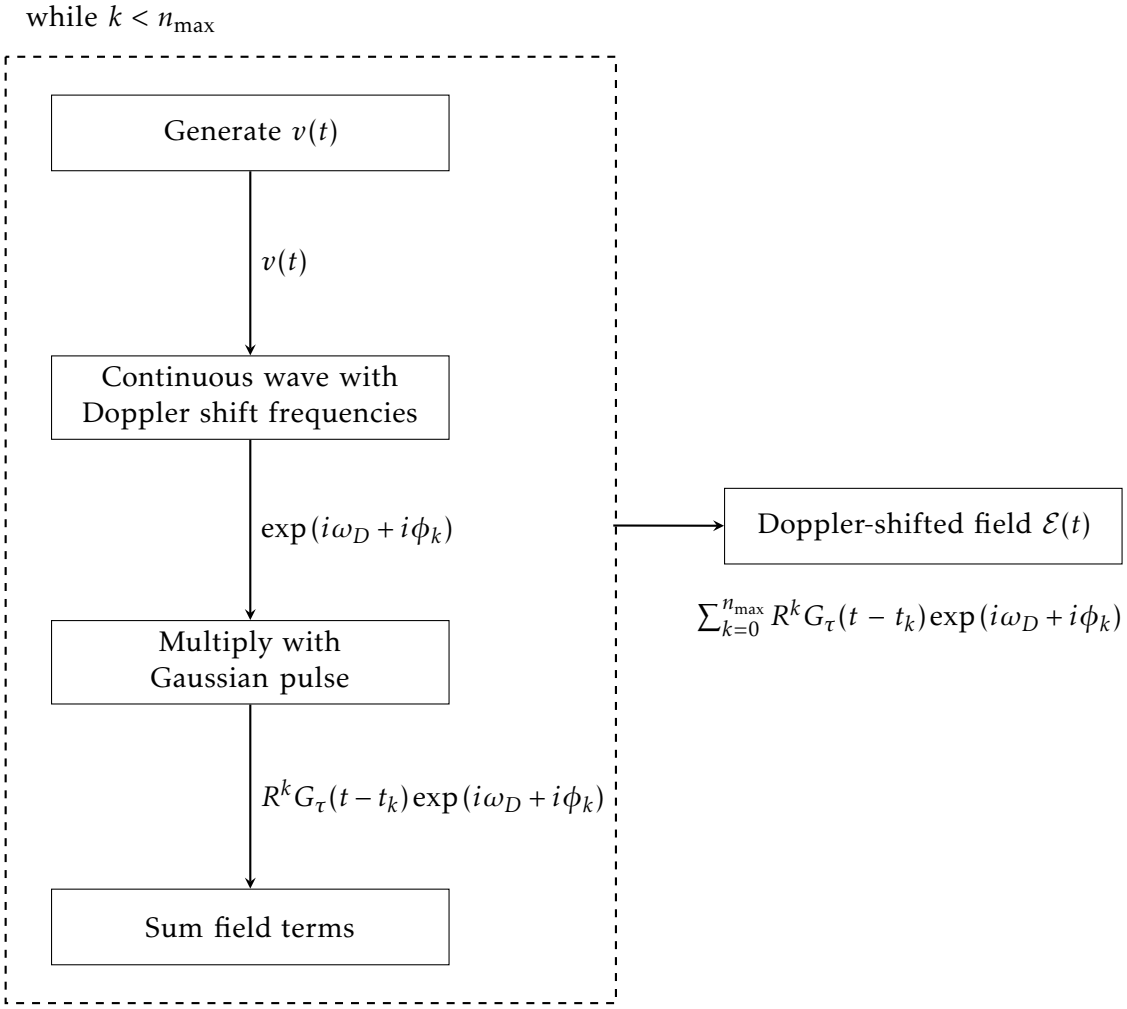

Figure 4.6: Diagram of the simulation process for the Doppler-shifted field. $n_{\max}$ represents the maximum number of reflections to consider and is given by equation (4.7).

4.4 Solving the Bloch equations

The populations after laser excitation from the simulated Doppler-shifted fields were obtained as numerical solutions of the Bloch equations (3.64) through an implementation of the Runge-Kutta fourth-order method.

The system of equations (3.64) can be written using the matrix notation of equation (3.20) as

$$\frac{\mathrm{d}\boldsymbol{\rho}}{\mathrm{d}t} = \boldsymbol{f}(t, \boldsymbol{\rho}) \qquad , \qquad \boldsymbol{\rho}(t_0) = \boldsymbol{\rho_0} \, , \tag{4.8}$$

with

$$\boldsymbol{\rho} = \begin{pmatrix} \rho_{11} \\ \rho_{22} \\ \rho_{12} \\ \rho_{21} \\ \rho_{33} \end{pmatrix} \quad , \quad \boldsymbol{f}(t,\boldsymbol{\rho}) = \begin{pmatrix} 0 & \Gamma_{sp} & \frac{i}{2}\mathcal{V}(t) & -\frac{i}{2}\mathcal{V}^*(t) & 0 \\ 0 & -\Gamma_{sp}-\Gamma_{inel} & -\frac{i}{2}\mathcal{V}(t) & \frac{i}{2}\mathcal{V}^*(t) & 0 \\ \frac{i}{2}\mathcal{V}^*(t) & -\frac{i}{2}\mathcal{V}^*(t) & i\Delta-\frac{\Gamma_c}{2} & 0 & 0 \\ -\frac{i}{2}\mathcal{V}(t) & \frac{i}{2}\mathcal{V}(t) & 0 & -i\Delta-\frac{\Gamma_c}{2} & 0 \\ 0 & \Gamma_{inel} & 0 & 0 & 0 \end{pmatrix} \begin{pmatrix} \rho_{11} \\ \rho_{22} \\ \rho_{12} \\ \rho_{21} \\ \rho_{33} \end{pmatrix}, \tag{4.9}$$

and

$$\boldsymbol{\rho_0} = \begin{pmatrix} \rho_{11}(t_0) \\ \rho_{22}(t_0) \\ \rho_{12}(t_0) \\ \rho_{21}(t_0) \\ \rho_{33}(t_0) \end{pmatrix} = \begin{pmatrix} 1 \\ 0 \\ 0+0i \\ 0+0i \\ 0 \end{pmatrix}, \tag{4.10}$$

as the initial value of the populations.

With the Runge-Kutta fourth-order method [48], the populations at a future time, t_{n+1}, can be calculated from the populations at $t = t_n$ as

$$\begin{aligned} \boldsymbol{\rho}(t_{n+1}) &= \boldsymbol{\rho}(t_n) + \frac{1}{6}\,\mathrm{d}t(\boldsymbol{k_1} + 2\boldsymbol{k_2} + 2\boldsymbol{k_3} + \boldsymbol{k_4})\,, \\ t_{n+1} &= t_n + \mathrm{d}t\,, \end{aligned} \tag{4.11}$$

with

$$\begin{aligned} \boldsymbol{k_1} &= \boldsymbol{f}(t_n, \boldsymbol{\rho}(t_n))\,, \\ \boldsymbol{k_2} &= \boldsymbol{f}(t_n + \frac{\mathrm{d}t}{2}, \boldsymbol{\rho}(t_n) + \mathrm{d}t\frac{\boldsymbol{k_1}}{2})\,, \\ \boldsymbol{k_3} &= \boldsymbol{f}(t_n + \frac{\mathrm{d}t}{2}, \boldsymbol{\rho}(t_n) + \mathrm{d}t\frac{\boldsymbol{k_2}}{2})\,, \\ \boldsymbol{k_4} &= \boldsymbol{f}(t_n + \mathrm{d}t, \boldsymbol{\rho}(t_n) + \mathrm{d}t\boldsymbol{k_3})\,, \end{aligned} \tag{4.12}$$

where $\mathrm{d}t$ is a chosen time interval corresponding to the step-size between iterations.

Applying this method to calculate the populations obtained for the simulated fields of figure 4.7(a) it is possible to visualize (see figure 4.7(b)) that the obtained populations have an inherent variance arising from the random nature of the generated electric fields.

In order to reduce the variance obtained when calculating the average population ($\overline{\rho_{33}}$) it is necessary to increase the number of simulated fields such that the resulting average population corresponds to that obtained for a field of fluence $\overline{\mathcal{F}}$, given by expression

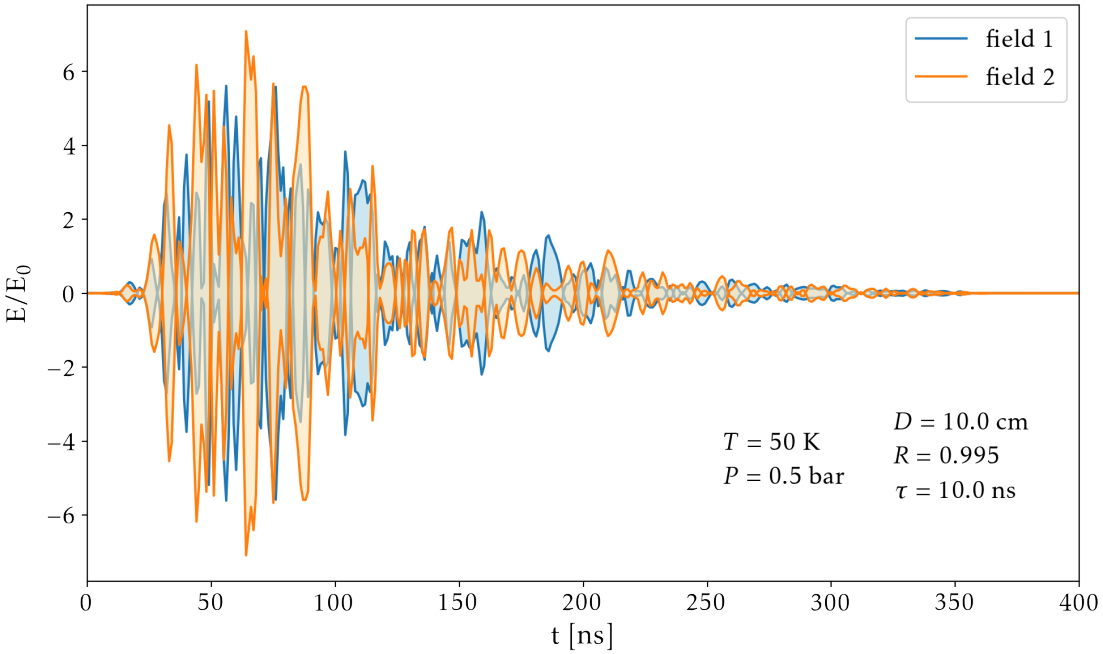

(a) Generated fields

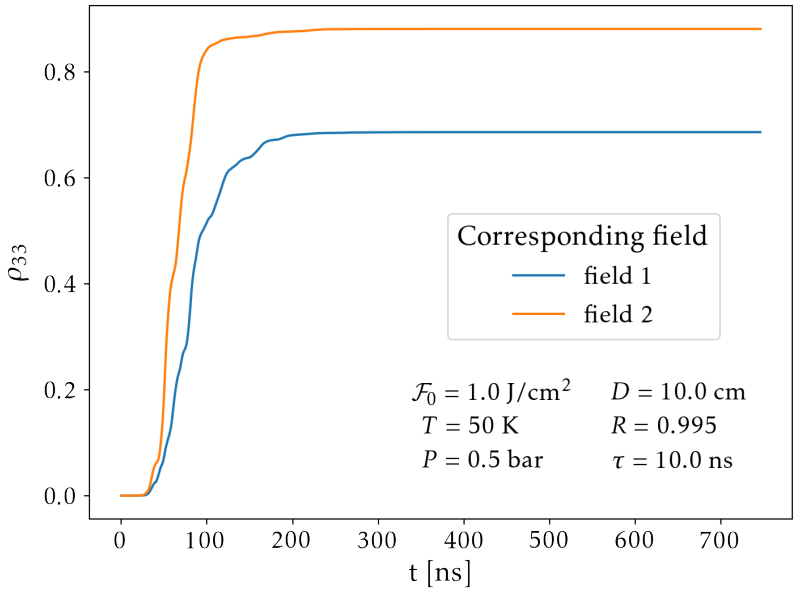

(b) Populations obtained from the generated fields.

Figure 4.7: Two fields and corresponding populations simulated for the same set of experimental conditions. The difference in the obtained results highlights the randomness introduced in the simulation by the random phases of the electric field pulses upon reflection.

(3.74). Figure 4.8 shows how the variance of $\overline{\rho_{33}}$ depends upon the number of simulated fields (n_{sim}) for a specific set of experimental conditions.

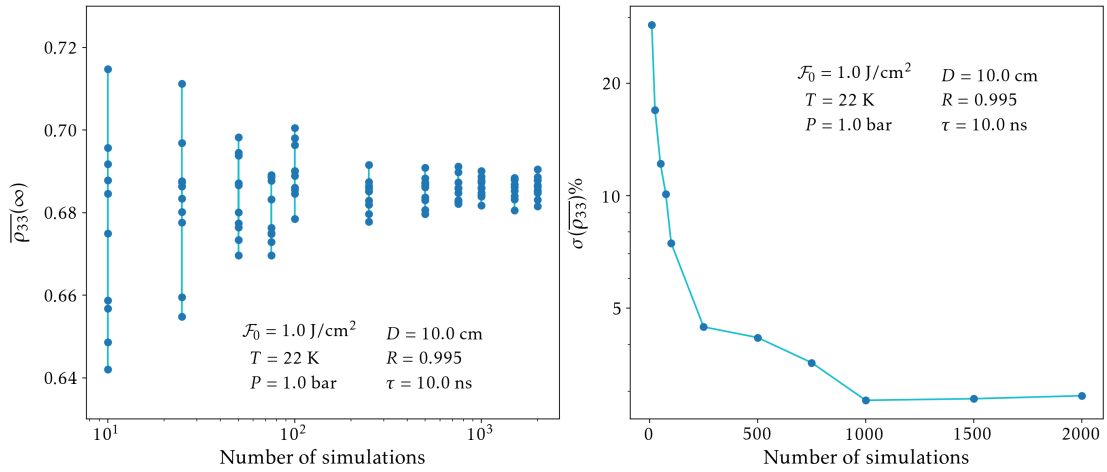

Figure 4.8: **Left** - Average population $\overline{\rho_{33}}$ for different number of simulated fields. **Right** - Percentage variance of $\overline{\rho_{33}}$ *vs.* number of simulated fields.

It is possible to see, in figure 4.8, that the percentage variance of $\overline{\rho_{33}}$ decreases drastically with the increase in number of simulations. In particular, from $n_{\text{sim}} = 10$ to $n_{\text{sim}} = 1000$ the observed variance drops from $\sim 30\%$ to $\sim 3\%$, while no significant difference is observed between the results obtained for 1000 and 2000 simulations.

Two factors contribute to the variance of the energy level populations obtained through the Doppler shift method. These are:

- The random phase upon reflection, which leads to a decoherent interference;
- The sampled velocities and collision times used in the construction of the velocity function $v(t)$.

Each of these factor varies differently under a change of the laser pulse and cavity parameters (τ, D, R), leading to different effects on the obtained population variance.

As it can be seen from the results presented in table 4.1, an increase of the laser pulse duration leads to a decrease of the population variance. This effect is the result of an increase in sample size for the sampled velocities and collision times, given that longer laser pulses allow for a larger number of collisions (velocity changes) during the laser pulse duration. As a larger sample size leads to a smaller statistical variance and the number of random phase shifts is independent of τ, the observed effect is expected. It can also be seen that higher cavity reflectivity values lead to smaller population variances. This effect is also caused by an increase of the sample size, given that higher reflectivity leads to an increase in the number of simulated reflections, as can be seen from equation (4.7). When the number of simulated reflections increases, both the velocity and phase shift sample sizes increase, leading to the smaller percentage variances observed.

Table 4.1: Population variance for various experimental conditions and $n_{\text{sim}} = 1000$.

τ [ns]	D [cm]	R	$\sigma(\overline{\rho_{33}})\%$
10	10	0.900	8.9
10	10	0.995	2.9
10	20	0.900	10.3
10	20	0.995	2.8
100	10	0.900	2.1
100	10	0.995	0.4
100	20	0.900	3.8
100	20	0.995	0.9

4.5 Performance and optimization

The simulation built for this work was entirely written in Python [46], which, being a high-level interpreted language, often leads to slow execution times. In order to optimize the simulation's runtime, two decorators from the library Numba [49], a Just-In-Time (JIT) compiler that converts Python-written functions into optimized machine code, were used. These decorators are:

- `@njit` - compiles the decorated function to run without accessing the Python interpreter leading to higher performance;
- `@vectorize` - transforms a regular Python function with scalar input arguments into a NumPy [50] universal function (ufunc) with equal performance as a traditional ufunc written in C.

For the functions where several cavity fields or populations are calculated in a loop, the decorator `@njit` was used with the keyword argument `(parallel=True)` such that these fields and populations can be calculated in parallel inside these loops (see listing A.11).

In table 4.2 several runtimes are presented for the generation of 1000 cavity fields and calculation of their associated populations at different experimental conditions, using an Intel® Core i5-3570 (3.4 GHz, 4 cores, 4 threads) CPU [51]. From the results of this table we see that an increase in the value of R leads to a significant increase of the runtime for generating the cavity electric fields. This is expected since a higher reflectivity leads to more reflections being calculated before reaching a defined minimum amplitude, as can be seen from equation (4.7). When compared to the field generation runtimes, no significant runtime increase is observed in the calculation of the associated populations.

Table 4.2: Runtime for generating the cavity electric fields and calculating the associated populations for different experimental conditions and $n_{sim} = 1000$. Simulations ran on an Intel® Core i5-3570 (3.4 GHz, 4 cores, 4 threads) CPU.

τ [ns]	D [cm]	R	field runtime [s]	population runtime [s]
10	10	0.900	0.6	0.8
10	10	0.995	19.2	1.4
10	20	0.900	0.6	0.9
10	20	0.995	29.5	2.0
100	10	0.900	1.3	1.7
100	10	0.995	32.8	2.3
100	20	0.900	1.2	1.7
100	20	0.995	41.3	2.8

4.6 Comparison with the convolution method

It is expected that the Doppler-shifted method produces the same Doppler-broadened energy level populations as the (most commonly used) convolution method. In order to ensure the validity of this new alternative method we compared the values of the μp resonance lineshape widths and steady-state energy level populations obtained with both methods, considering constant amplitude fields of different fluences at the temperatures of 22 K and 50 K. The obtained results are presented in table 4.3 and an example resonance lineshape obtained through the Doppler shift method is shown in figure 4.9.

Table 4.3: Comparison of the μp resonance lineshape widths and steady-state energy level populations obtained with the convolution and Doppler shift methods for constant amplitude electric fields. Γ_{conv} and ρ_{33}^{conv} represent the lineshape widths and resonant ($\Delta = 0$) steady-state populations obtained through the convolution method of section 3.2.3 while Γ_{DS} and $\overline{\rho_{33}}$ represent the average lineshape widths and resonant steady-state populations obtained through the Doppler shift method with $n_{sim} = 1000$. A laser pulse duration of 100 ns and a pressure of 0.5 bar where considered. All collisional rates where obtained from table 3.1 considering a statistical distribution for the H_2 rotational levels.

T [K]	F [J/cm^2]	Γ_{conv} [MHz]	Γ_{DS} [MHz]	ρ_{33}^{conv}	$\overline{\rho_{33}}$
22	10	241	249	0.18	0.18
	20	242	258	0.32	0.32
	50	243	285	0.60	0.62
50	10	253	259	0.18	0.19
	20	254	268	0.31	0.33
	50	258	292	0.53	0.59

From the data presented in table 4.3 it is possible to see that both methods produce agreeing results for lower values of laser fluence (10 J/cm^2 and 20 J/cm^2), with some deviation occurring for larger fluences ($F = 50$ J/cm^2). For the steady-sate populations,

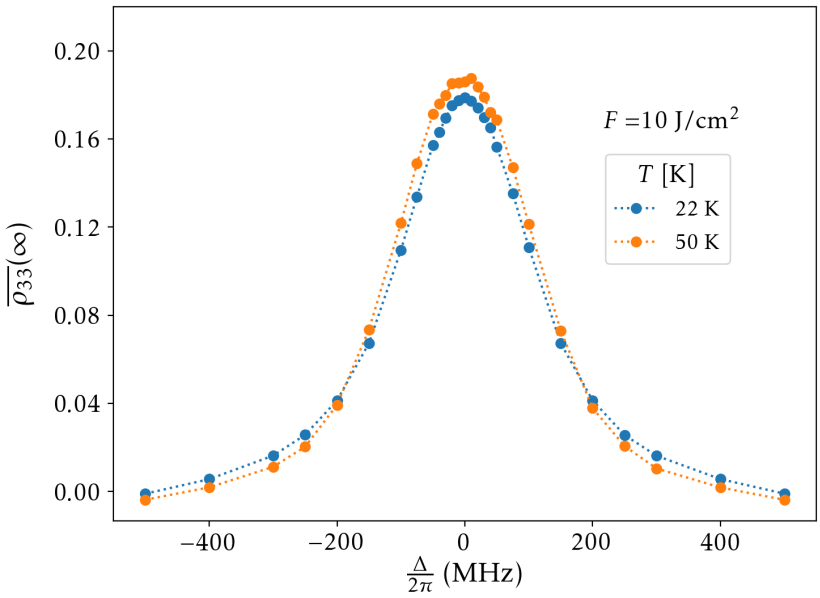

Figure 4.9: Resonance lineshapes obtained through the Doppler shift method for a constant amplitude laser field of 10 J/cm^2 fluence and 100 ns duration at the temperatures of 22 K and 50 K and 0.5 bar pressure. Both lineshapes were calculated with $n_{\text{sim}} = 1000$ and all collision rates were obtained from table 3.1 considering a statistical distribution for the H_2 rotational levels.

an average relative error of 4% was obtained with the largest contribution coming from the values calculated for $T = 50$ K and $F = 50$ J/cm^2 which presented a 12% error relative to the populations obtained through the convolution method. A larger relative error was observed for the resonance lineshape widths (8%), with the largest contribution coming also from the higher values of laser fluence.

The Doppler shift method was therefore demonstrated to be accurate for calculating the resonant ($\Delta = 0$) steady-state energy level populations, especially for lower values of laser fluence, with a larger inaccuracy observed in the calculation of the lineshape widths. The results presented in chapter 5 are therefore focused on the simulation of these steady-state populations at different experimental conditions, considering the modeled electric field inside the laser cavity. A more extensive study on the μp energy level populations and resonance lineshapes for constant amplitude fields can be found in [33].

5

Results and Discussion

In order to study the dependence of the μp energy level populations upon certain experimental conditions, the simulation described in chapter 4 was used to obtain these populations for several sets of:

- Temperature and pressure of the H_2 gas inside the laser cavity
- Laser cavity diameter and pulse duration
- Laser fluence and effective cavity reflectivity.

Through all the simulations performed in this work, the laser is assumed to be on resonance ($\omega = \omega_r$) and have a negligible bandwidth. The rate of spontaneous emission is neglected ($\Gamma_{sp} = 0$) since $\Gamma_{el} \ll \Gamma_c$ for the considered experimental conditions (see table 3.2).

5.1 Temperature and pressure conditions

To understand the effect of the H_2 gas temperature (T) on the average steady state population of the quenched level ($\overline{\rho_{33}}$), a simulation was performed for the temperatures of 22 K and 50 K at a constant value of pressure and three different values of laser fluence. The results of this simulation, plotted in figure 5.1 and written in table 5.1, show that a change of temperature from 22 K to 50 K leads to a slight increase in the obtained steady-state populations.

While a higher temperature leads to a wider Doppler width (Γ_D) and therefore to a smaller steady-state population, from table 3.1 we see that an increase in temperature at constant pressure implies a decrease in density, leading to smaller collision rates, which in turn lead to a higher steady-state population, as shown in figure 3.13(a). The trade-off between these two opposite effects leads to the small variations observed for these two values of temperature [33].

For the study of the effect of the H_2 gas pressure (P) on the steady-state population, a second simulation was performed for the pressures of 0.5 bar, 1.0 bar and 2.0 bar at a fixed temperature of 50 K and the same three values of laser fluence. The results of

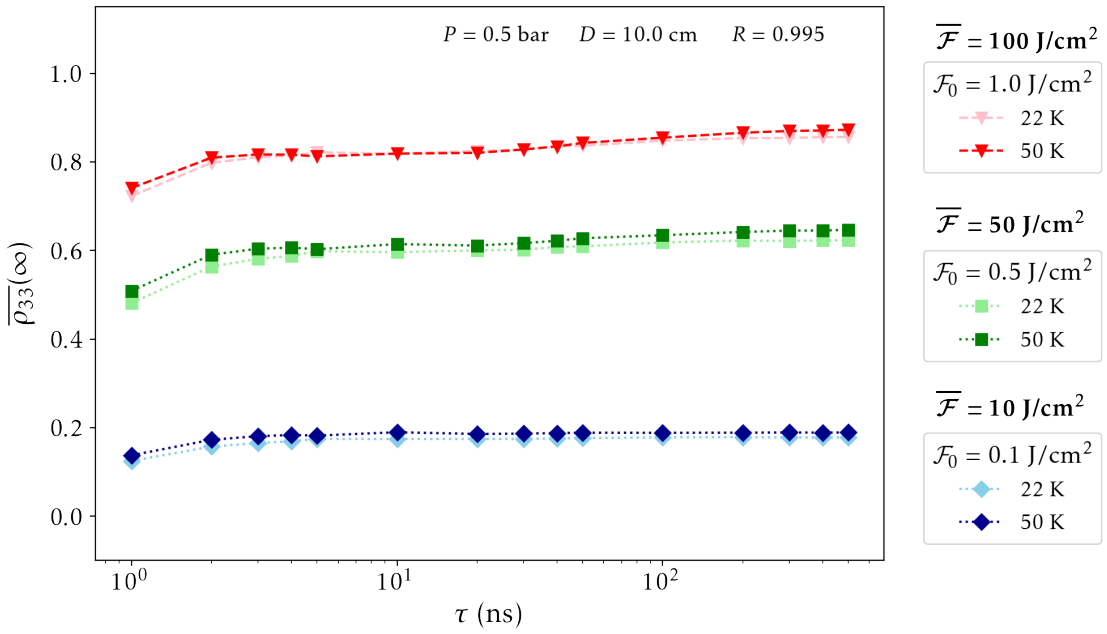

Figure 5.1: Average population for different values of fluence and temperature. Each plotted point is the result of a simulation with $n_{\text{sim}} = 1000$. Collisional rates obtained from table 3.1 assuming a statistical distribution for the H_2 rotational levels.

Table 5.1: Populations obtained for different values of pulse duration, fluence and temperature with $P = 0.5$ bar, $D = 10$ cm, $R = 0.995$ and $n_{\text{sim}} = 1000$. . Collisional rates obtained from table 3.1 assuming a statistical distribution for the H_2 rotational levels.

τ [ns]	$\mathcal{F}$ [J/cm^2]	T [K]	$\overline{\rho_{33}}$
10	100	22	0.82
10	100	50	0.82
10	50	22	0.60
10	50	50	0.61
10	10	22	0.17
10	10	50	0.19
100	100	22	0.85
100	100	50	0.86
100	50	22	0.62
100	50	50	0.63
100	10	22	0.18
100	10	50	0.19

this simulation are plotted in figure 5.2 and show that an increase in pressure leads to a decrease in the obtained steady-state populations. This effect is expected since table 3.1 shows that an increase in pressure leads to higher collisional rates.

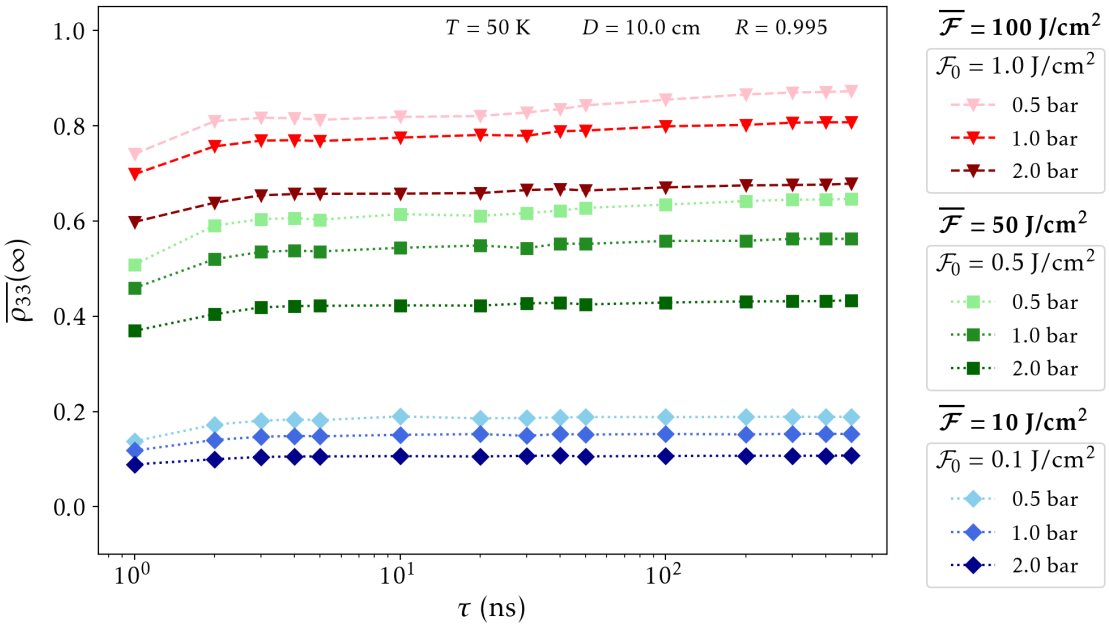

Figure 5.2: Average population for different values of fluence and pressure. Each plotted point is the result of a simulation with $n_{\text{sim}} = 1000$. Collisional rates obtained from table 3.1 assuming a statistical distribution for the H_2 rotational levels.

Higher values of laser fluence, for the same temperature and pressure conditions, lead to a smaller value of the ratio $\Gamma_c/\mathcal{V}_0^2\mathcal{F}_0$. This, in turn, leads the behavior of the steady-state population towards the Rabi oscillation regime, discussed in section 3.4.2, which explains the increase in oscillations observed for the higher values of laser fluence in figures 5.1 and 5.2.

5.2 Cavity geometry

The novelty in this work, relative to previous studies [33] on the population of the HFS energy levels of μp, is the possibility for a better understanding of the effects of the cavity's diameter (D) and reflectivity (R) on these populations, through the use of the modeled Doppler-shifted field, defined in section 3.3.

Figure 5.3 shows the results of two simulations where the steady-state populations were obtained in function of the cavity's diameter, D, for different values of laser fluence and pulse duration. These results show that for higher fluences and shorter pulse durations, a decrease in cavity diameter leads to lower average steady-state populations.

The observed effect is expected and can be better understood through the data listed

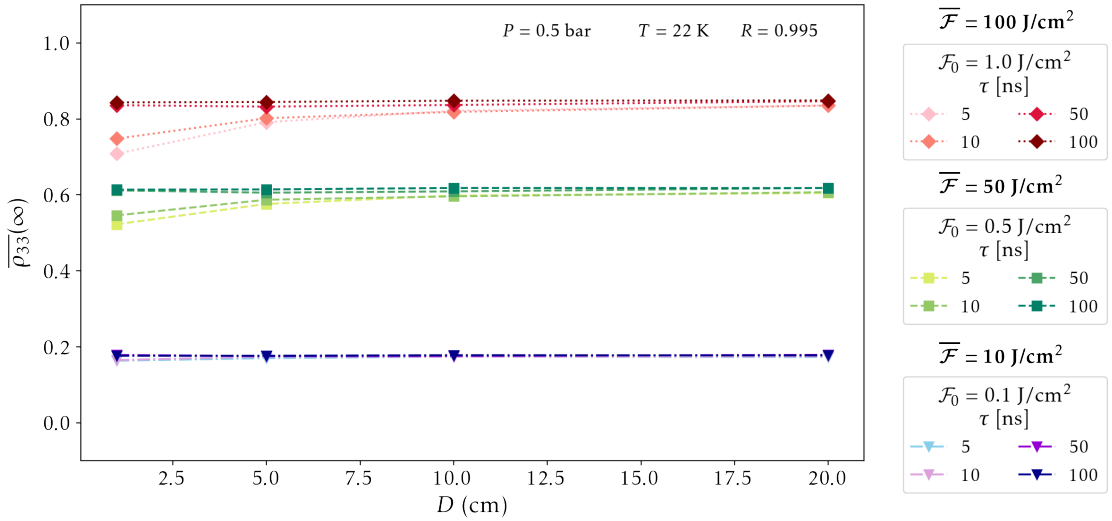

(a) $T = 22$ K

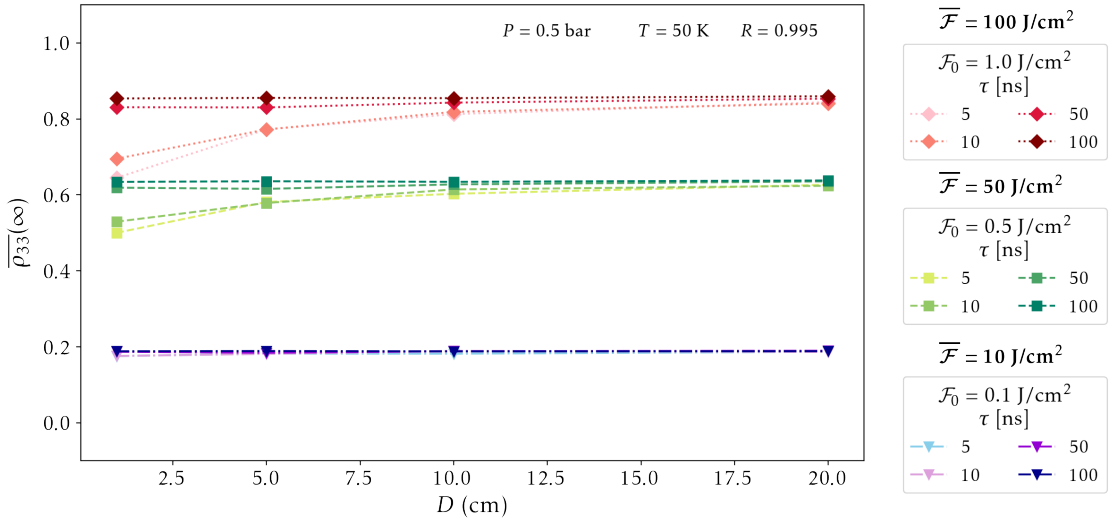

(b) $T = 50$ K

Figure 5.3: Average population *vs.* cavity diameter for different values of fluence and pulse duration. Each plotted point is the result of a simulation with $n_{\text{sim}} = 1000$. Collisional rates obtained from table 3.1 assuming a statistical distribution for the H_2 rotational levels

in table 5.2, where the quantity Δt represents the travel time between two subsequent reflections for a given cavity diameter, for a laser pulse traveling with speed c. It is possible to see that the percentage change in the quantity $\Delta t/\tau$, relating the travel time and the laser pulse duration, is much greater for lower values of τ. Therefore, the change in the superposition of subsequent reflections, caused by a decrease of the cavity diameter, is much greater for short duration pulses, leading to the smaller steady-state populations obtained for these pulses.

Table 5.2: Populations obtained for different values of pulse duration and cavity diameter, with $\mathcal{F}_0 = 1.0$ J/cm^2, $T = 50$ K, $P = 0.5$ bar, $R = 0.995$ and $n_{\text{sim}} = 1000$. Collisional rates obtained from table 3.1 assuming a statistical distribution for the H_2 rotational levels.

τ [ns]	D [cm]	Δt [ns]	$\Delta t/\tau$ (%)	$\overline{\rho_{33}}$
5	1	0.03	0.67	0.64
10	1	0.03	0.33	0.70
50	1	0.03	0.07	0.83
100	1	0.03	0.03	0.85
5	5	0.17	3.34	0.77
10	5	0.17	1.67	0.77
50	5	0.17	0.33	0.83
100	5	0.17	0.17	0.86
5	10	0.33	6.67	0.81
10	10	0.33	3.34	0.82
50	10	0.33	0.67	0.84
100	10	0.33	0.33	0.85
5	20	0.67	13.34	0.84
10	20	0.67	6.67	0.84
50	20	0.67	1.33	0.85
100	20	0.67	0.67	0.86

5.3 Cavity reflectivity and laser fluence

The relation between the laser's initial fluence ($\mathcal{F}_0$), the pulse duration (τ) and the cavity's reflectivity (R) is given by equations (3.74) and (3.72), with an effect on the Rabi frequency given by equation (3.75). As can be seen from those equations, it is possible to achieve a given value of the average fluence inside the laser cavity ($\overline{\mathcal{F}}$) with many different combinations of $\mathcal{F}_0$ and R. However, the steady-state populations are determined not by the value of $\overline{\mathcal{F}}$ but by the time-dependent Rabi frequency, which also depends upon the laser pulse duration, given the normalization constant of equation (3.58).

To visualize how the steady-state population behaves under different combinations of $\mathcal{F}_0$ and R, two simulations where performed for the temperatures of 22 K and 50 K, where three values of $\overline{\mathcal{F}}$ are obtained through four combinations of $\mathcal{F}_0$ and R for a range of laser pulse durations. The results of these simulations are plotted in figure 5.4.

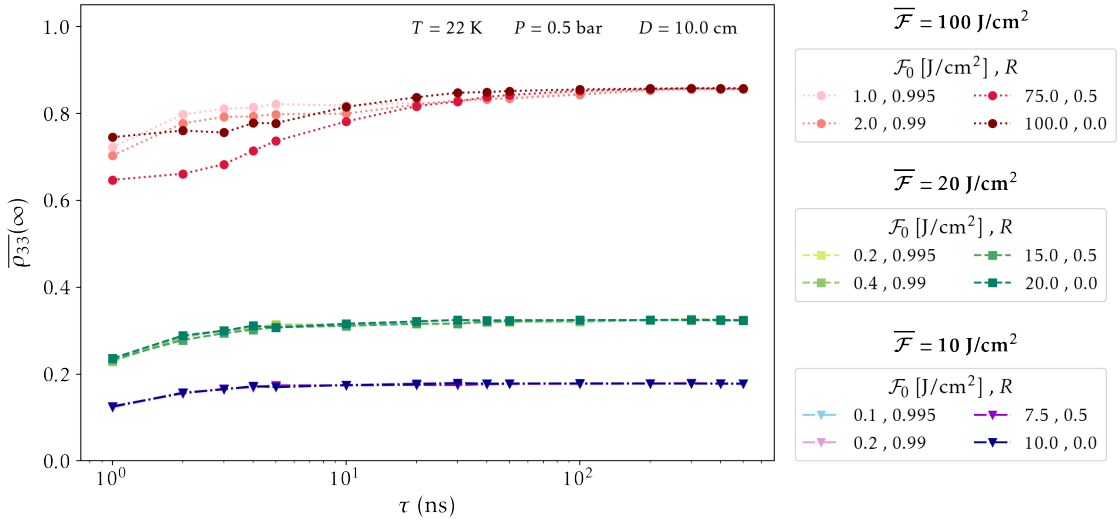

(a) $T = 22$ K

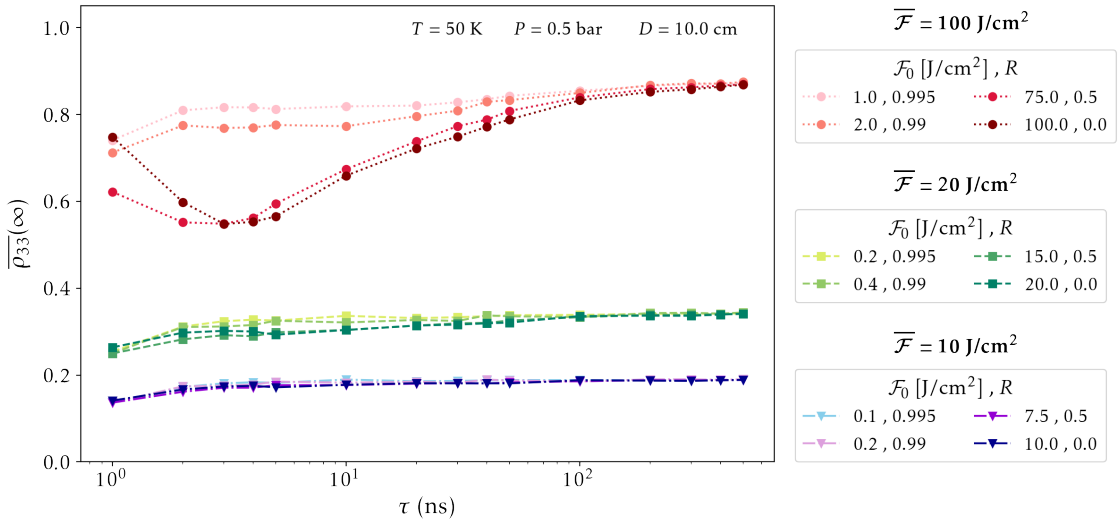

(b) $T = 50$ K

Figure 5.4: Average population *vs.* pulse duration for different values of fluence obtained with several combinations of initial pulse fluence and cavity reflectivity. Each plotted point is the result of a simulation with $n_{\text{sim}} = 1000$. Collisional rates obtained from table 3.1 assuming a statistical distribution for the H_2 rotational levels

From the results of figure 5.4 we see that for a low average total fluence (10 J/cm^2, 20 J/cm^2), all the chosen combinations of initial pulse fluence and reflectivity tend to produce the same steady-state populations for the same values of laser pulse duration, with a common decrease observed for the values of $\tau < 3$ ns. However, for higher fluences (100 J/cm^2) the steady-state populations obtained for high initial pulse fluence and low cavity reflectivity tend to deviate from those obtained for lower initial pulse fluence and high reflectivity as the pulse duration decreases. This effect is explained by equation (3.75), from where it is possible to see that increasing values of $\mathcal{F}_0$ lead to higher Rabi frequencies which in turn lead the system towards the Rabi oscillation regime, causing the steady state population to oscillate with the value of τ, as shown in figure 3.13(b). The observed oscillations are greater for a temperature of 50 K compared to those obtained for 22 K which can be explained by the decrease in the collision rates, Γ_{el} and Γ_{inel}, with increasing temperature. Smaller collision rates result in a smaller decoherence rate, Γ_c, which leads the system towards greater amplitude oscillations, given the smaller value of the ratio $\Gamma_c/\mathcal{V}_0\mathcal{F}_0$.

6

Conclusions

In light of the upcoming HyperMu experiment of the CREMA collaboration, a simulation method was developed in order to obtain the probability of laser excitation and following collisional de-excitation of a μp atom in an H_2 gas mixture. The implemented simulation allows for the calculation of this probability to account for collisional and Doppler effects while the μp atoms are under the influence of a modeled electric field that depends upon the laser properties and cavity conditions, such as pulse duration, fluence, mirror reflectivity and cavity diameter. The collisional effects are directly introduced into the three-level Bloch equations through the use of broadening ratios while the Doppler, laser and cavity geometry effects are included in the Bloch equations via a time-dependent Rabi frequency defined by a simulated Doppler-shifted electric field. In addition, the use of a simulated Doppler-shifted field provided faster calculations of the Doppler broadened energy level populations obtained from the Bloch equations by allowing the calculation of these populations at specific values of the laser frequency detune, without the need of a convolution integral.

The probability of collisional quenching after laser excitation was simulated for several sets of experimental conditions, with results that provide both visualization and quantification of how this probability varies under different conditions of pressure, temperature, cavity geometry, reflectivity and laser pulse fluence and duration. In particular, the results obtained for different values of the cavity diameter show that, for a fluence of 100 J/cm^2, a decrease of the cavity diameter from 10 cm to 1 cm leads to a decrease as high as 21% for the probability of a μp atom to reach the desired quenched state, revealing the importance of the laser cavity conditions included in the model of the effective shape of the electric field. A difference of only 5% was observed when considering the same variation of diameter with the more expected experimental condition of 10 J/cm^2 for the HyperMu experiment.

All the obtained results where interpreted under the study of the Bloch equations for different dimensionless broadening ratios, providing a theoretical framework that may be useful for future studies on the probability of excitation of similar atomic systems.

Bibliography

[1] J. M. Lourenço, *The NOVAthesis LaTeX Template User's Manual*, NOVA University Lisbon, 2021. [Online]. Available: https://github.com/joaomlourenco/novathesis/raw/master/template.pdf.

[2] K. Jungmann, "Laser spectroscopy of muonic atoms", *Zeitschrift für Physik C Particles and Fields*, vol. 56, no. 1, S59–S69, Mar. 1992, ISSN: 1431-5858. DOI: 10.1007/BF02426776. [Online]. Available: https://doi.org/10.1007/BF02426776.

[3] M. I. Eides, H. Grotch, and V. A. Shelyuto, "Theory of light hydrogenlike atoms", *Physics Reports*, vol. 342, no. 2, pp. 63–261, 2001, ISSN: 0370-1573. DOI: https://doi.org/10.1016/S0370-1573(00)00077-6. [Online]. Available: https://www.sciencedirect.com/science/article/pii/S0370157300000776.

[4] A. Antognini, F. Kottmann, F. Biraben, P. Indelicato, F. Nez, and R. Pohl, "Theory of the 2s–2p lamb shift and 2s hyperfine splitting in muonic hydrogen", *Annals of Physics*, vol. 331, pp. 127–145, 2013, ISSN: 0003-4916. DOI: https://doi.org/10.1016/j.aop.2012.12.003. [Online]. Available: https://www.sciencedirect.com/science/article/pii/S0003491612002102.

[5] S. G. Karshenboim, "Precision physics of simple atoms: Qed tests, nuclear structure and fundamental constants", *Physics Reports*, vol. 422, no. 1, pp. 1–63, 2005, ISSN: 0370-1573. DOI: https://doi.org/10.1016/j.physrep.2005.08.008. [Online]. Available: https://www.sciencedirect.com/science/article/pii/S0370157305003637.

[6] R. Pohl *et al.*, "The size of the proton", *Nature*, vol. 466, no. 7303, pp. 213–216, Jul. 2010, ISSN: 1476-4687. DOI: 10.1038/nature09250. [Online]. Available: https://doi.org/10.1038/nature09250.

[7] A. Antognini *et al.*, "Proton structure from the measurement of 2s-2p transition frequencies of muonic hydrogen", *Science (New York, N.Y.)*, vol. 339, pp. 417–20, Jan. 2013. DOI: 10.1126/science.1230016.

[8] A. Antognini, *Muonic atoms and the nuclear structure*, 2016. arXiv: 1512.01765 [physics.atom-ph].

[9] A. Beyer *et al.*, "The rydberg constant and proton size from atomic hydrogen", *Science*, vol. 358, no. 6359, pp. 79–85, 2017, ISSN: 0036-8075. DOI: 10.1126/science.aah6677. eprint: https://science.sciencemag.org/content/358/6359/79.full.pdf. [Online]. Available: https://science.sciencemag.org/content/358/6359/79.

[10] H. Fleurbaey *et al.*, "New measurement of the 1s-3s transition frequency of hydrogen: Contribution to the proton charge radius puzzle", *Physical review letters*, vol. 120, no. 18, p. 183 001, 2018.

[11] N. Bezginov, T. Valdez, M. Horbatsch, A. Marsman, A. C. Vutha, and E. A. Hessels, "A measurement of the atomic hydrogen lamb shift and the proton charge radius", *Science*, vol. 365, no. 6457, pp. 1007–1012, 2019, ISSN: 0036-8075. DOI: 10.1126/science.aau7807. eprint: https://science.sciencemag.org/content/365/6457/1007.full.pdf. [Online]. Available: https://science.sciencemag.org/content/365/6457/1007.

[12] G. Lee, J. R. Arrington, and R. J. Hill, "Extraction of the proton radius from electron-proton scattering data", *Physical Review D*, vol. 92, no. 1, Jul. 2015, ISSN: 1550-2368. DOI: 10.1103/physrevd.92.013013. [Online]. Available: http://dx.doi.org/10.1103/PhysRevD.92.013013.

[13] J. Arrington and I. Sick, "Evaluation of the proton charge radius from electron–proton scattering", *Journal of Physical and Chemical Reference Data*, vol. 44, no. 3, p. 031 204, 2015.

[14] W. Xiong *et al.*, "A small proton charge radius from an electron–proton scattering experiment", *Nature*, vol. 575, no. 7781, pp. 147–150, Nov. 2019, ISSN: 1476-4687. DOI: 10.1038/s41586-019-1721-2. [Online]. Available: https://doi.org/10.1038/s41586-019-1721-2.

[15] A. Grinin *et al.*, "Two-photon frequency comb spectroscopy of atomic hydrogen", *Science*, vol. 370, no. 6520, pp. 1061–1066, 2020. DOI: 10.1126/science.abc7776. eprint: https://www.science.org/doi/pdf/10.1126/science.abc7776. [Online]. Available: https://www.science.org/doi/abs/10.1126/science.abc7776.

[16] H. Gao and M. Vanderhaeghen, *The proton charge radius*, 2021. arXiv: 2105.00571 [hep-ph].

[17] C. Peset, A. Pineda, and O. Tomalak, "The proton radius (puzzle?) and its relatives", *Progress in Particle and Nuclear Physics*, vol. 121, p. 103 901, 2021, ISSN: 0146-6410. DOI: https://doi.org/10.1016/j.ppnp.2021.103901. [Online]. Available: https://www.sciencedirect.com/science/article/pii/S0146641021000600.

[18] R. Pohl *et al.*, "Laser spectroscopy of muonic deuterium", *Science*, vol. 353, no. 6300, pp. 669–673, 2016, ISSN: 0036-8075. DOI: 10.1126/science.aaf2468. eprint: https://science.sciencemag.org/content/353/6300/669.full.pdf. [Online]. Available: https://science.sciencemag.org/content/353/6300/669.

[19] T. Nebel *et al.*, "The lamb-shift experiment in muonic helium", *Hyperfine Interactions*, vol. 212, no. 1, pp. 195–201, Dec. 2012, ISSN: 1572-9540. DOI: 10.1007/s10751-012-0637-0. [Online]. Available: https://doi.org/10.1007/s10751-012-0637-0.

[20] J. J. Krauth *et al.*, "Measuring the α-particle charge radius with muonic helium-4 ions", *Nature*, vol. 589, no. 7843, pp. 527–531, Jan. 2021, ISSN: 1476-4687. DOI: 10.1038/s41586-021-03183-1. [Online]. Available: https://doi.org/10.1038/s41586-021-03183-1.

[21] R. Pohl *et al.*, *Laser spectroscopy of muonic atoms and ions*, 2016. arXiv: 1609.03440 [physics.atom-ph].

[22] E. Cherednikova, R. Faustov, and A. Martynenko, "Proton polarizability contribution to the hyperfine splitting in muonic hydrogen", *Nuclear Physics A*, vol. 703, no. 1, pp. 365–377, 2002, ISSN: 0375-9474. DOI: https://doi.org/10.1016/S0375-9474(01)01461-0. [Online]. Available: https://www.sciencedirect.com/science/article/pii/S0375947401014610.

[23] C. E. Carlson, V. Nazaryan, and K. Griffioen, "Proton-structure corrections to hyperfine splitting in muonic hydrogen", *Phys. Rev. A*, vol. 83, p. 042 509, 4 Apr. 2011. DOI: 10.1103/PhysRevA.83.042509. [Online]. Available: https://link.aps.org/doi/10.1103/PhysRevA.83.042509.

[24] C. Peset and A. Pineda, "The two-photon exchange contribution to muonic hydrogen from chiral perturbation theory", *Nuclear Physics B*, vol. 887, pp. 69–111, 2014, ISSN: 0550-3213. DOI: https://doi.org/10.1016/j.nuclphysb.2014.07.027. [Online]. Available: https://www.sciencedirect.com/science/article/pii/S0550321314002466.

[25] F. Hagelstein, R. Miskimen, and V. Pascalutsa, "Nucleon polarizabilities: From compton scattering to hydrogen atom", *Progress in Particle and Nuclear Physics*, vol. 88, pp. 29–97, 2016, ISSN: 0146-6410. DOI: https://doi.org/10.1016/j.ppnp.2015.12.001. [Online]. Available: https://www.sciencedirect.com/science/article/pii/S0146641015001118.

[26] C. Peset and A. Pineda, "Model-independent determination of the two-photon exchange contribution to hyperfine splitting in muonic hydrogen", *Journal of High Energy Physics*, vol. 2017, no. 4, p. 60, Apr. 2017, ISSN: 1029-8479. DOI: 10.1007/JHEP04(2017)060. [Online]. Available: https://doi.org/10.1007/JHEP04(2017)060.

[27] J. M. Alarcón, F. Hagelstein, V. Lensky, and V. Pascalutsa, "Forward doubly-virtual compton scattering off the nucleon in chiral perturbation theory. ii. spin polarizabilities and moments of polarized structure functions", *Phys. Rev. D*, vol. 102, p. 114 026, 11 Dec. 2020. DOI: 10.1103/PhysRevD.102.114026. [Online]. Available: https://link.aps.org/doi/10.1103/PhysRevD.102.114026.

[28] V. Punjabi, C. F. Perdrisat, M. K. Jones, E. J. Brash, and C. E. Carlson, *The structure of the nucleon: Elastic electromagnetic form factors*, 2015. arXiv: 1503.01452 [nucl-ex].

[29] J. C. Bernauer *et al.*, "Electric and magnetic form factors of the proton", *Phys. Rev. C*, vol. 90, p. 015 206, 1 Jun. 2014. DOI: 10.1103/PhysRevC.90.015206. [Online]. Available: https://link.aps.org/doi/10.1103/PhysRevC.90.015206.

[30] X. Zhan *et al.*, "High-precision measurement of the proton elastic form factor ratio $\mu_p G_E/G_M$ at low Q^2", *Physics Letters B*, vol. 705, no. 1, pp. 59–64, 2011, ISSN: 0370-2693. DOI: https://doi.org/10.1016/j.physletb.2011.10.002. [Online]. Available: https://www.sciencedirect.com/science/article/pii/S0370269311012342.

[31] I. Sick and D. Trautmann, "Proton root-mean-square radii and electron scattering", *Phys. Rev. C*, vol. 89, p. 012 201, 1 Jan. 2014. DOI: 10.1103/PhysRevC.89.012201. [Online]. Available: https://link.aps.org/doi/10.1103/PhysRevC.89.012201.

[32] G. K. Woodgate, *Elementary Atomic Structure*, 2nd ed. Oxford University Press, USA, 1983, ISBN: 0198511566.

[33] P. Amaro *et al.*, "Laser excitation of the 1s-hyperfine transition in muonic hydrogen", *in preparation*,

[34] W. R. Johnson, *Atomic Structure Theory: Lectures on Atomic Physics*. Springer-Verlag Berlin Heidelberg, 2007, ISBN: 978-3-540-68013-0. [Online]. Available: https://www.springer.com/gp/book/9783540680109.

[35] J. Schwinger, L. Deraad, K. Milton, W. Tsai, and J. Norton, *Classical Electrodynamics*, ser. Advanced book program. Avalon Publishing, 1998, ISBN: 9780813346625. [Online]. Available: https://books.google.pt/books?id=SVz%5C_lRkP09kC.

[36] L. Sustelo, "Role of polarization in laser spectroscopy of the hyperfine ground state in muonic hydrogen and helium-3", *in preparation*,

[37] S. Schmidt *et al.*, "The next generation of laser spectroscopy experiments using light muonic atoms", vol. 1138, p. 012 010, Nov. 2018. DOI: 10.1088/1742-6596/1138/1/012010. [Online]. Available: https://doi.org/10.1088/1742-6596/1138/1/012010.

[38] Paul Sherrer Institut, *Measurement of the hyperfine splitting in muonic hydrogen and laser technology*, Available at: https://www.psi.ch/en/ltp/hypermu. Last Accessed on 24-11-2021.

[39] W. E. Lamb and R. C. Retherford, "Fine structure of the hydrogen atom by a microwave method", *Phys. Rev.*, vol. 72, pp. 241–243, 3 Aug. 1947. DOI: 10.1103/PhysRev.72.241. [Online]. Available: https://link.aps.org/doi/10.1103/PhysRev.72.241.

[40] J. L. Friar, "Nuclear finite-size effects in light muonic atoms", *Ann. Phys. (N.Y.); (United States)*, vol. 122:1, Sep. 1979. DOI: 10.1016/0003-4916(79)90300-2. [Online]. Available: https://www.osti.gov/biblio/5842396.

[41] R. Loudon, *The Quantum Theory of Light*, 3rd ed. OUP Oxford, 2000, ISBN: 9780191589782. [Online]. Available: https://books.google.pt/books?id=AEkfajgqldoC.

[42] P. Courteille, *Atom-light interaction and basic applications*, Available at: https://www.ifsc.usp.br/~strontium/Publication/Scripts/LightAtomsLecture.pdf, 2021.

[43] A. Adamczak, "Differential cross sections for muonic atom scattering from hydrogenic molecules", *Phys. Rev. A*, vol. 74, p. 042718, 4 Oct. 2006. DOI: 10.1103/PhysRevA.74.042718. [Online]. Available: https://link.aps.org/doi/10.1103/PhysRevA.74.042718.

[44] F. Mandl, *Statistical Physics*, 2nd ed., ser. Manchester Physics Series. Wiley, 2013, ISBN: 0471915335. [Online]. Available: https://books.google.pt/books?id=ZMSNPFrfaU8C.

[45] D. Bakalov and M. Stoilov, "Toward the measurement of the hyperfine structure of muonic hydrogen in the famu experiment: Multi-pass cavity optimization for experiments with pulsed sources.", *EPJ Web of Conferences*, vol. 181, p. 01 033, 2018. DOI: 10.1051/epjconf/201818101033. [Online]. Available: https://doi.org/10.1051/epjconf/201818101033.

[46] P. S. Foundation, *Python language reference*, Available at: https://www.python.org/.

[47] R. Yates and D. Goodman, *Probability and Stochastic Processes: A Friendly Introduction for Electrical and Computer Engineers*. John Wiley & Sons, 2005, ISBN: 9780471452591. [Online]. Available: https://books.google.pt/books?id=sWNnQgAACAAJ.

[48] P. L. DeVries and J. Hasbun, *A First Course in Computational Physics*. Jones & Bartlett Learning, 2011, ISBN: 9780763773144. [Online]. Available: https://books.google.fr/books?id=X3FEPiebLHOC.

[49] S. K. Lam, A. Pitrou, and S. Seibert, "Numba: A llvm-based python jit compiler", in *Proceedings of the Second Workshop on the LLVM Compiler Infrastructure in HPC*, ser. LLVM '15, Austin, Texas: Association for Computing Machinery, 2015, ISBN: 9781450340052. DOI: 10.1145/2833157.2833162. [Online]. Available: https://doi.org/10.1145/2833157.2833162.

[50] C. R. Harris *et al.*, "Array programming with numpy", *Nature*, vol. 585, no. 7825, pp. 357–362, Sep. 2020, ISSN: 1476-4687. DOI: 10.1038/s41586-020-2649-2. [Online]. Available: https://doi.org/10.1038/s41586-020-2649-2.

[51] Intel Corporation, *Intel® core™ i5-3570 processor specifications*, Available at: https://ark.intel.com/content/www/us/en/ark/products/65702/intel-core-i5-3570-processor-6m-cache-up-to-3-80-ghz.html. Last Accessed on 24-11-2021.

A

Code

The written code is divided into five scripts:

- `constants.py` - definition of physical constants and unit conversions;
- `maxwell.py` - Maxwell-Boltzmann statistics and random paths;
- `field.py` - functions for simulating the electric field inside the laser cavity;
- `blochRK4.py` - defining and solving the Bloch equations for the generated electric fields through the Runge-Kutta fourth-order method;
- `fileIO.py` - functions for reading/writting the simulated results into `.out` files.

The main functions from each of these scripts are listed in this appendix. Most of these functions rely on the Numpy [50] and Numba [49] libraries.

A.1 `constants.py`

```
'''
A list of:
-Physical constants
-Important constant values (masses, matrix elements, etc.)
-Conversions
'''

e = 1.60217662E-19 # electron charge (C)
eps0 = 8.8541878128E-12 # vaccuum permittivity (F/m)

kB = 1.3806E-23 # boltzmann constant (J/K)
kB_eV = kB/e # boltzmann constant (eV/K)

u = 1.66054E-27 # 1 Dalton (kg)
m_mu = 0.1134289*u # muon mass (kg)
m_p = 1.00726467*u # proton mass (kg)
m_muH = m_mu + m_p #muH mass - no binding energy (kg)
```

```
m_H2 = 1.00784*u # H2 mass (kg)

c = 299792458 # speed of light (m/s)
hbar = 1.054571800E-34 #reduced Planck constant (SI)

LHD = 4.25E22 # liquid hydrogen density (at/cm^3)

MM1 = 1.228E-15 # magnetic dipole matrix element for muH HFS (m)

#conversions

bar2Pa = 1.0E5 # bar to Pa conversion
```

Listing A.1: Python script with declared physicasl constants and unit conversions.

A.2 maxwell.py

```
@njit
def MB_velocity(m, T, size=None):
    '''
    Maxwell-Boltzmann velocity generator
    Samples an array of velocities from a MB distribution
    for given mass and temperature

    Input

    m - mass of the particles in kg
    T - temperature in K
    size - size of the array (number of velocities to generate)

    Return

    numpy array with the generated velocities
    '''

    sigma = np.sqrt(ct.kB*T/m) #standard deviation of the 1D MB dist

    return np.random.normal(loc=0, scale=sigma, size=size)
```

Listing A.2: Implemented function for sampling velocities components from a one-dimensional Maxwell-Boltzmann velocity distribution.

```
@njit
def random_velocities(t, m, T, collision_rate):
    '''
    Generates MB velocities for Poisson sampled collisions

    Input

```

```
    t - time array to calculate the velocties for
    m - mass of the particles in kg
    T - temperature in K
    collision_rate - collision rate of the particles at given temperature

    Return

    v_arr - numpy array with v values for all values of t
    t_ind - indicies of t where a collision happened
    '''

    dt = t[1]-t[0]
    v_arr = np.zeros(shape=len(t)) #empty v(t)
    t_ind = [0] #array with the time indices where collisions happened (also
                                        includes the indices 0 and len(t))

    v = MB_velocity(m, T, size=1)[0]
    p = dt*collision_rate

    v_arr[0] = v # first 2 instances of velocity
    v_arr[1] = v

    for i in range(2, len(t)-2):

        n = np.random.random()

        if n<p and i>t_ind[-1]+1: #imediate successive collisions are not
                                        allowed
            v = MB_velocity(m, T, size=1)[0]
            t_ind.append(i)

        v_arr[i] = v

    v_arr[-2] = v
    v_arr[-1] = v

    t_ind.append(len(t))

    return v_arr, t_ind
```

Listing A.3: Algorithm for generating random path velocities with collision times following a Poisson distribution.

A.3 field.py

```
@vectorize
def gauss(t, t0, tau):
    '''
    Gausian pulse

    Input

    t - time value
    t0 - center of the Gaussian pulse
    tau - width (standard deviation) of the Gaussian pulse

    Return

    Gaussian pulse value at t

    '''

    if np.abs(t-t0) > 5*tau:
        return 0.0
    else:
        x = (t - t0)/tau
        return np.exp(-(1/2)*x**2)
```

Listing A.4: Function for generating a Gaussian pulse using the decorator `@vectorize` from the Numba library.

```
@njit
def t_maxn_dopp(tau, t0, D, R, minAmp):
    '''
    Calculates the max number of reflections and time needed
    for a Doppler-shifted cavity field

    Input

    tau - duration of the initial Gaussian pulse
    t0 - center of the initial Gaussian pulse
    D - cavity diameter
    R - cavity reflectance
    minAmp - minimum amplitude to consider (between 0.0 and 1.0)

    Return

    t - numpy array with the time values
    maxN - maximum reflection to calculate according to minAmp
    '''

    maxN = int(np.log(minAmp)/np.log(R)) #max reflections
```

```
22
23      #these values were determined by analyzing several results
24      if tau < 15E-9:
25          t_cushion = 300E-9
26      else:
27          t_cushion = 0.0
28
29      # the values 10*tau and 5*tau where determined by analyzing several
                                            results
30      if tau <= 100.0E-9:
31          tmax = t0 + maxN*(D/ct.c) + 10*tau + t_cushion
32      else:
33          tmax = t0 + maxN*(D/ct.c) + 5*tau + t_cushion
34
35      dt = 1.0E-9 #limit for sampling of Doppler frequency f*v/c (assuming v <=
                                            1000 m/s)
36
37      t = np.arange(0.0, tmax, dt)
38
39      return t, maxN
```

Listing A.5: Function for calculating the maximum number of reflections and the time interval to consider when generating a Doppler-shifted field.

```
1   @njit
2   def doppler_wave(t, m, T, collision_rate, freq, phase):
3       '''
4       Generates a continuous wave that changes frequency
5       according to collision times sampled from
6       a Poisson distribution (from maxwell.random_velocities)
7
8       The frequencies considered are Doppler-shifted
9       according to particle velocity
10
11      Input
12
13      t - numpy array with time values
14      m - mass of the particle (for random_velocities)
15      T - temperature (for random_velocities)
16      collision_rate - collision rate (for random_velocities)
17      freq - frequency of the laser (not shifted)
18      phase - initial phase of the wave
19
20      Return
21
22      wave - numpy aray with the wave function for all times t
23      '''
24
25      v_arr, t_ind = mx.random_velocities(t, m, T, collision_rate) #velocities
                                            and collision times
```

```
    freq_arr = freq*v_arr/ct.c #Doppler-shifted frequencies

    phi = phase #initial phase
    wave = np.zeros(shape=len(t), dtype=np.csingle)
    wave[t_ind[0]:t_ind[1]] = np.exp(1j*freq_arr[t_ind[0]]*t[t_ind[0]:t_ind[1]
                                        ] + 1j*phi)

    for i in range(1, len(t_ind)-1):

        ind_0 = t_ind[i]
        ind_1 = t_ind[i+1]

        prev_freq = freq_arr[ind_0-1]
        new_freq = freq_arr[ind_0]

        phi = (prev_freq-new_freq)*t[ind_0] + phi
        wave[ind_0:ind_1] = np.exp(1j*new_freq*t[ind_0:ind_1] + 1j*phi)

    return wave
```

Listing A.6: Function for generating a continuous wave with Doppler-shifted frequencies changing according to collision times obtained from the algorithm of listing A.3.

```
@njit
def cavityField_dopp(tau, t0, D, R, minAmp, m, T, collision_rate, carrier_freq
                                        ):
    '''
    Simulates the Doppler-shifted electric field inside the laser cavity

    Input

    tau - duration of the initial Gaussian pulse
    t0 - center of the initial Gaussian pulse
    D - cavity diameter
    R - cavity reflectance
    minAmp - minimum amplitude to consider (between 0.0 and 1.0)
    m - mass of the particle
    T - temperature in K
    collision_rate - collision rate
    carrier_freq - frequency of the laser

    Return

    field - numpy array with the complex valued Doppler shifted cavity field
                                        amplitude
    t - numpy array with the time values (from t_maxn function)
    maxN - max reflection calculated (from t_maxn function)
    '''

    t, maxN = t_maxn_dopp(tau, t0, D, R, minAmp)
```

```
26
27      phi = np.random.uniform(0.0, 2*np.pi, size=maxN) #random phases
28
29      field = np.zeros(shape=len(t), dtype=np.csingle)
30
31      for i in range(maxN):
32
33          wave_dopp = doppler_wave(t, m, T, collision_rate, carrier_freq, phi[i]
                                     )
34          field += (R**i)*gauss(t, t0+i*(D/ct.c), tau)*wave_dopp
35
36      field = normConst_gaussSq(tau)*field #normalization
37
38      return field, t, maxN
```

Listing A.7: Algorithm for simulating a Doppler-shifted cavity field.

A.4 blochRK4.py

```
1  @njit
2  def rabiFreq(field, F, M):
3      '''
4      Calculates the rabi frequency for a given
5      complex field amplitude, fluence and matrix element
6
7      Input
8
9      field - complex valued field amplitude
10     F - laser fluence
11     M - transition matrix element
12
13     Return
14
15     rabi frequency
16     '''
17
18     return M*(ct.e/ct.hbar)*np.sqrt(2*F/(ct.eps0*ct.c))*np.conjugate(field)
```

Listing A.8: Function for calculating the Rabi frequency given a dimensionless Doppler-shifted field $\mathcal{E}$.

```
1  @njit
2  def blochField_3lvl(t, rho, rabi, params):
3      '''
4      Defines the Bloch equations for the 3-level system of muH HFS
5      1S(F=0), 1S(F=0) + Kinetic energy, 1S(F=1)
6
7      Input
8
```

```
    t - time values
    rho - array with all populations and coherences to calculate (rho11, rho12
                                        , rho22, rho33)
    rabi - rabi frequency
    params - paramaters (detune, spont. emission, el. collision, inel.
                                        collision)

    Return

    array with Bloch equations (eq11, eq12, eq22, eq33)
    '''

    detune = params[0]
    gamma_sp = params[1]
    gamma_el = params[2]
    gamma_inel = params[3]

    gamma_p = gamma_sp #population broadening
    gamma_c = gamma_sp + gamma_el + gamma_inel #coherence broadening

    #rho = np.array([rho11, rho12, rho22, rho33])

    eq11 = -np.imag(rabi*rho[1]*np.exp(1j*detune*t)) + gamma_p*rho[2]
    eq12 = (1j/2)*np.conjugate(rabi)*(rho[0]-rho[2])*np.exp(-1j*detune*t)-(
                                        gamma_c/2)*rho[1]
    eq22 = -eq11 - gamma_inel*rho[2]
    eq33 = gamma_inel*rho[2]

    rho_dot = np.array([eq11, eq12, eq22, eq33])

    return rho_dot
```

Listing A.9: Function for defining the three-level Bloch equations (3.42) with a given Doppler-shifted field.

```
@njit
def solveBlochRK4_field_3lvl(t, rabi, params, bound):
    '''
    Solves the Bloch equations numerically with Runge-Kutta (4th order) method

    Input

    t - time values
    rabi - rabi frequency
    params - parameters (detune, spont. emission, el. collision, inel.
                                        collision)
    bound - initial conditions for all populations and coherences

    Return

```

```
    numpy array with values of all populations and coherences for all times t
    '''

    nt = len(t)
    t0 = t[0]
    dt = t[1]-t0

    nx = len(bound)
    x = np.zeros(shape=(nx, nt), dtype=bound.dtype)
    x[:,0] = bound

    for i in range(nt-1):

        k1 = dt*blochField_3lvl(t[i], x[:,i], rabi[i], params)
        k2 = dt*blochField_3lvl(t[i] + dt/2, x[:,i] + k1/2, rabi[i], params)
        k3 = dt*blochField_3lvl(t[i] + dt/2, x[:,i] + k2/2, rabi[i], params)
        k4 = dt*blochField_3lvl(t[i] + dt, x[:,i] + k3, rabi[i], params)

        dx = (k1 + 2*k2 + 2*k3 + k4)/6

        x[:,i+1] = x[:,i] + dx

    return x
```

Listing A.10: Algorithm for solving the three-level Bloch equations (3.42) with the Runge-Kutta fourth-order method.

```
@njit(parallel = True)
def solveAverage_field_3lvl(t, rabi, params, bound, nsim):
    '''
    Solves the Bloch equations numerically with Runge-Kutta (4th order) method
    The equations are solved several times in a cycle (in parallel)
    for an array of different time-dependent rabi frequencies
    to obtain an average population

    Input

    t - time values
    rabi - rabi frequency
    params - parameters (detune, spont. emission, el. collision, inel.
                                        collision)
    bound - initial conditions for all populations and coherences
    nsim - number of cycles (must be <= len(rabi))

    Return

    average populations and coherences for all times t
    '''

    rho = np.zeros(shape=(nsim, len(bound), len(t)), dtype=bound.dtype)
```

```
23
24      for i in prange(nsim):
25          rho[i] = solveBlochRK4_field_3lvl(t, rabi[i], params, bound)
26
27      return np.sum(rho, axis=0)/nsim
```

Listing A.11: Algorithm for calculating the average populations and coherences from the three-level Bloch equations (3.42) with the Runge-Kutta fourth-order method. The decorator `@njit(parallel=True)` causes the for-loop with `prange` to be run in parallel.

A.5 fileIO.py

```
1  def write_fields_dopp(path, fields, T, P, tau, D, R):
2      '''
3      Function for writing an array of Doppler-shifted
4      cavity fields to an .out file
5
6      Input
7
8      path - path of the file to write on
9      fields - numpy array with complex valued doppler-shifted cavity field
                                          amplitudes
10     T - temperature for which the field was calculated
11     P - temperature for which the field was calculated
12     tau - pulse duration
13     D - cavity diameter
14     R - cavity reflectance
15
16     The file is named as fields_dopp_T_P_tau_D_R.out
17     where T is in K, P is in bar/10, tau is in ns, D in cm
18     and R is a value between 0 and 1000
19
20     e.g.
21     T = 50.0 K
22     P = 0.5 bar
23     tau = 10.0 ns
24     D = 10.0 cm
25     R = 0.995
26
27     fields_dopp_50_5_10_10_995.out
28     '''
29
30     name_f = f'fields_dopp_{int(T)}_{int(P*10/ct.bar2Pa)}_{int(tau*1E9)}_{int(
                                          D*1E2)}_{int(R*1000)}.out'
31
32     with open(os.path.join(path, name_f), 'w') as f:
33         np.savetxt(f, fields)
34
```

```
35
36 def read_fields_dopp(path, T, P, tau, D, R):
37     '''
38     Function for reading an array of Doppler-shifted
39     cavity fields from an .out file
40
41     Input
42
43     path - path of the file to write on
44     T - temperature for which the field was calculated
45     P - temperature for which the field was calculated
46     tau - pulse duration
47     D - cavity diameter
48     R - cavity reflectance
49
50     Return
51
52     Efield_arr - numpy array with complex valued doppler-shifted
53     cavity field amplitudes
54     '''
55
56     name_f = f'fields_dopp_{int(T)}_{int(P*10/ct.bar2Pa)}_{int(tau*1E9)}_{int(
                                        D*1E2)}_{int(R*1000)}.out'
57
58     with open(os.path.join(path, name_f), 'r') as f:
59         Efield_arr_str = np.loadtxt(f, dtype=str)
60         Efield_arr = np.zeros(shape=Efield_arr_str.shape, dtype=np.csingle)
61         for i in range(len(Efield_arr)):
62             Efield_arr[i] = np.array([np.complex(x) for x in Efield_arr_str[i]
                                        ])
63
64     return Efield_arr
```

Listing A.12: Functions for reading/writing the generated Doppler-shifted fields from/into .out files.